Cellulose
https://doi.org/10.1007/s10570-025-06862-8

ORIGINAL RESEARCH

X-ray diffraction combined analysis method for the determination of cellulose crystal ultrastructure for free and deformed flax fibre bundles

Magali Morales · Komlavi Gogoli · Daniel Chateigner · Luca Lutterotti · Christophe Poilâne · Florian Gehring · Gregory Stoclet · Olivier Perez

Received: 6 May 2025 / Accepted: 13 November 2025

Abstract In this work, we propose an X-ray diffraction characterization of the flax ultrastructure to improve our understanding of its role in expressing the complex mechanical behaviour of flax fibres. Initially, X-ray diffraction measurements were performed on both undeformed and deformed samples consisting in fibre bundles and using for the first time, the combined "structure/microstructure/texture" analysis method implemented in the Maud software and based on a Rietveld algorithm. For all the fibre bundles, the microstructural analysis showed that these microfibrils, having a cellulose Iβ structure, exhibit an ellipsoidal crystallite shape elongated along their c-axis. The results also suggest the existence of a paracrystalline cellulose phase in the flax ultrastructure, with a degree of order intermediate between amorphous and crystalline Iβ cellulose. The corresponding quantitative texture analysis allowed to access the microfibril angle distribution in the flax secondary wall, with cellulose microfibrils inclined with respect to fibre axes with angles in the 0–20° range and a maximum of the distribution around 5°–10°. The combination of tensile tests and in-situ X-ray diffraction measurements put in evidence a substantial rearrangement of the microfibril angle distribution confirming the reorientation of cellulose microfibrils along the fibre axis. However, this evolution is non-linear and appears significant for deformations below 0.6%, becoming relatively weak or attenuated for higher deformations. This X-ray combined analysis provides new insights into the organization of cellulose in flax fibres, and by extension, plant fibres in general.

Keywords Flax fibre · X-ray diffraction · Cellulose · Microfibril angle · Combined analysis method · Quantitative texture analysis · Anisotropic size

M. Morales (✉) · K. Gogoli · C. Poilâne · F. Gehring
Laboratoire CIMAP–Ensicaen, UNICAEN, CEA, CNRS, 6 Bd du Maréchal Juin, 14050 Caen, France
e-mail: magali.morales@ensicaen.fr; magali.morales@unicaen.fr

D. Chateigner · O. Perez
Laboratoire CRISMAT–Ensicaen, UNICAEN, CNRS, 6 Bd du Maréchal Juin, 14050 Caen, France

L. Lutterotti
Department of Industrial Engineering, University of Trento, 38123 Trento, Italy

G. Stoclet
UMET–Unité Matériaux et Transformations, Univ. Lille, CNRS, INRAE, Centrale Lille, 59000 Lille, France

Introduction

To address current climate challenges, the implementation of production methods that are more environmentally friendly and aligned with sustainable development is strongly advocated by various protocols (Kyoto, 1997) and international agreements (Paris Agreement, 2015). Therefore, as part of a global strategy to reduce the environmental impact

Published online: 19 November 2025

of industrial processes, plant fibres such as flax are set to play a key role in the production of bio-based materials (Gomez-Campos et al. 2021). However, plant fibres such as flax and hemp exhibit non-linear mechanical behaviour, which is often explained by the morphology, biochemical composition or ultrastructure of the elementary fibres. Regarding the latter point, flax fibre has a complex ultrastructural organization whose role in the expression of mechanical behaviour remains to be elucidated.

The structure of flax reveals a multiscale organization at four levels (Richely et al. 2021a): macroscopic, mesoscopic, microscopic and nanoscopic. At the mesoscopic scale, fibre bundles have an average thickness of around 100 μm (Garat et al. 2018; Gogoli et al. 2021; Haag and Müssig 2016) and are composed of 10–40 elementary fibres (Charlet et al. 2007). At the microscopic scale, elementary fibres are bound by a middle lamella of amorphous, polymer-rich pectins, usually between 10 and 30 µm thick (Baley 2002; Baley and Bourmaud 2014). The cross-section of the fibre exhibits a circular or elliptical channel called a lumen, whose cross-section area represents on average 0.5 to 10.3% of the total cross-section area (Aslan et al. 2011; Charlet et al. 2010a, 2010b; Richely et al. 2021b). Finally, at the nanoscopic scale, the elementary fibre wall is organized into several layers. The primary wall is the outer wall, with a thickness between 0.1 and 0.5μm (Baley et al. 2005; Clair et al. 2018; Gorshkova et al. 2018; Melelli et al. 2020a; Rihouey et al. 2017). The secondary, or inner wall, has a thickness around 8–10 μm and is made up of three concentric layers. From the outside to the inside, we distinguish: the S_1 layer with a thickness between 0.5 and 5μm, the S_2 layer—called G in some studies—with a thickness between 5 and 10 μm and the S_3 layer—called G_n in some studies – in the 0.5—1μm range (Clair et al. 2018; Gorshkova et al. 2018; Melelli et al. 2020a; Rihouey et al. 2017). Depending on the layer, considering flax fiber, semi-crystalline cellulose microfibrils, the most rigid elements of the cell wall, are arranged helically around the longitudinal axis of the fibre at an angle known as the Microfibril Angle (MFA), while embedded in a matrix of amorphous polymers: hemicelluloses, pectins and lignins. The S_2 layer, whose thickness represents 70–80% of the elementary fibre (Gorshkova and Morvan 2006; Morvan et al 2003) and contains between 75 and 90% cellulose, is considered to be largely responsible for the fibre's mechanical behaviour (John & Thomas 2008; Raj et al. 2011; Morgillo et al. 2025). The MFA, which ranges from 3–10° in S2 (Bourmaud et al. 2013; Muller et al. 1998; Wang et al 2020) is much larger and more dispersed in the S_1 and S_3 layers (between 30 and 70°) than is S_2 (Roland et al. 1995).

The major component of flax, cellulose, is known into four phases (I, II, III and IV), with the native form, cellulose I, found in plant fibres such as flax. It is composed of two distinct allomorphs, cellulose Iα possessing a single-chain triclinic structure and cellulose Iβ possessing a two-chain monoclinic structure (Nishiyama et al. 2002, 2003). According to Atalla and VanderHart (1999) and Jarvis (2003), cellulose Iβ accounts for 75% of the cellulose in plant fibres, the remaining 25% being cellulose Iα. In most studies, however, it is customary to consider the presence of cellulose Iβ alone whose crystal lattice parameters are shown in Table 1. In the walls, thanks to intermolecular hydrogen bonds, neighbouring cellulose chains agglomerate with each other to form cellulose microfibrils within which semicrystallinity results in an alternation between less ordered, less dense amorphous regions and more ordered crystalline regions (De Souza Lima & Borsali 2004; Saxena and Brown 2005).

The MFA in the S2 layer has a major influence on the mechanical behaviour of plant fibres (Placet et al. 2013; Placet et al. 2014a, b; Morgillo et al. 2025). Since cellulose is the most rigid element of the cell wall, understanding its organization in terms of orientation, microstructure (crystallite size and shape) and crystalline structure is essential to provide relevant answers to the link between ultrastructure and mechanical behaviour of flax fibres. A detailed understanding of the phenomena taking place at this scale is an essential step towards understanding the macroscopic mechanical behaviour of plant fibres. For this purpose, various methods have been reported in the literature such as X-ray diffraction (Bourmaud et al

Table 1 Lattice parameters of cellulose Iβ (Nishiyama et al. 2002, 2003) – COD number 4114994 (Gražulis et al. 2009)

Cell parameters (Å)			Angles (°)		
a	*b*	*c*	*α*	*β*	*γ*
7.784	8.201	10.38	90	90	96.5

2013; Kölln et al. 2005; Placet et al. 2011b), Nuclear magnetic resonance (NMR) spectroscopy (Bourmaud et al. 2019; Duchemin et al. 2012; Zuckerstätter et al. 2009), Raman spectroscopy (Agarwal 2009; Gierlinger et al. 2010), and various types of microscopy (scanning electron microscopy (SEM) (Richely et al. 2021b; Thygesen et al. 2007), atomic force microscopy (AFM) (Melelli et al. 2020b, 2021; Richely et al. 2021b), polarized light microscopy (PLM) (Donaldson and Xu 2005; L. G. Thygesen et al. 2007), transmission electron microscopy (Donaldson and Xu, 2005; Wardrop and Presto, 1947), fluorescence microscopy (Long et al. 1998; Mart, 1955). Among all these methods, X-ray diffraction, being a robust non-destructive method, is often used to characterize the ultrastructure of plant fibres, particularly semi-crystalline cellulose. It can be used to assess the crystallographic structure, phases, crystal sizes and microstrains, preferred orientation and chemical composition of materials exhibiting crystalline structures.

Historically, X-ray diffraction has been used to better understand the orientation of microfibrils by obtaining average MFA values of plant fibres. Depending on the wave vector range needed to be investigated, two types of techniques are used: wide- and small-angle X-ray Scattering (WAXS and SAXS resp.). With WAXS, Cave's usual method provides average MFA values from the width of the (200) reflection arc of the crystalline cellulose, which represents the planes parallel to the microfibril axes sometimes complemented by the (004) reflections (Cave 1997a, 1997b). With SAXS, the equatorial streak width is used to determine the MFA especially in secondary cell walls of flax fibers. In the case of wood cell walls, the simulated azimuthal SAXS signal has shown the existence of MFA distributions in primary S1 cell walls (Saxe et al. 2014). Moreover, recent studies using second harmonic generation microscopy have revealed locally variable MFA along the elementary fibre, primarily ranging from 0 to 10° for the S2 cell flax fibres, with an average of approximately 5° (Melelli et al. 2020a). These findings challenge the notion of a single MFA and instead suggest a distribution of MFA within a range of values. These points hold particular significance and warrant further investigation. For instance, gaining insights into the true distribution of MFA values within the cell wall would enable numerical models simulating the mechanical behaviour of fibres to be more accurate. X-ray diffraction also has the advantage of being combinable with other characterization techniques for in situ testing. Thus, by coupling X-ray diffraction and tensile tests, it is possible to monitor ultrastructure rearrangements under mechanical loading. In situ monitoring of MFA has been carried out (Placet et al. 2011a; Thuault 2011) on plant fibres, and shows a decrease in MFA during tensile loading.

In the context previously described, the objective of this study is to characterize the ultrastructure of flax, specifically semi-crystalline cellulose. This approach aims to gain a better understanding of the organization of flax cellulose, particularly the orientation of cellulose microfibrils, and to provide insights into its evolution during a tensile test. In this work, this characterization was achieved through X-ray diffraction. The parameters under investigation include structure, microstructure of crystallites (crystallite sizes, shapes and microstrains), texture (preferred orientation), and crystallinity. Adequate quantification of all these parameters enables their study evolution during an in situ tensile test.

Thus, initially, X-ray diffraction measurements were conducted on samples of non-deformed bundles of flax fibres and then on samples deformed during an in situ tensile test. These measurements were subsequently processed using, for the first time, the so-called Combined Analysis "structure/microstructure/texture" method [Chateigner et al. 2019], which facilitated, among other things, the determination of the MFA distribution, the shape and size of cellulose crystallites thus opening new perspectives regarding the characterization and understanding of the crystallinity of flax. Comparing the results of the measurement series performed on non-deformed and tension-deformed samples will allow for tracking the evolution of the ultrastructure of flax fibres during tensile loading.

Materials and methods

Materials

The flax fibre bundles used in this study were provided by the Natup company (Mont Saint Aignan, France) and originated from diverse flax varieties and batches. Standard processing steps for plant fibres, including retting, scutching, and combing,

were carried out. Notably, these bundles underwent a unique treatment involving water spraying to enhance the flexibility of natural pectins constituting the interfacial lamella of the elementary fibres within the bundle, facilitating their use as adhesive between numerous parallel bundles to create a cohesive roll. In the context of the research, bundles were extracted by hand at random from the roll, with meticulous care taken to prevent any damage during the extraction process. The use of fibre bundles is justified by the fact that they are easier to handle, thanks to their larger diameter compared with elementary fibres.

Experimental diffraction setups

Two series of X-ray diffraction measurements were carried out on two different diffractometers.

Measurement Series 1: Undeformed samples (S1_i samples with i in the 1–5 range and S2_j samples with j in the 1–7 range;Table 1).

Four non-deformed samples were measured using a Rigaku diffractometer, Oxford Diffraction model, with a microsource operating at 40 kV and 40mA (with monochromatized $CuK\alpha_{12}$ radiation) and equipped with a 2D image plate detector (Dectris Eiger R 1 M), using a sample-to-detector distance of 40 mm at room temperature. The parallel X-ray beam obtained from a pinhole size of 100 µm, hit the sample perpendicularly to the longitudinal axis (Fig. 1a), this latter being held in a U-shaped sample holder (Fig. 1b). The length of the sample is 30 mm A total of 180 diffraction images was acquired for 240 s each, using a φ-scan in the 0–360° range with a step of 2°, each image covering a 2θ angular range from 0 to 55° (Fig. 1a).

Because of geometrical limitations associated with this diffractometer and the traction device on the sample holder, the second series of measurements on deformed samples had to be operated on another diffractometer.

Measurement Series 2: Measurement on 3 different samples (S2_4, S2_5, S2_6) in the undeformed and deformed state (Table 2).

The main objective of this second series of measurements is to monitor in-situ the ultrastructural rearrangements of flax fibre bundles under tensile load. For this purpose, a micro-traction sample holder was designed (Fig. 2a), enabling mechanical traction under the X-ray diffraction beam. Diffraction measurements were carried out using this instrument on four samples not subjected to tensile stress, and on three samples that underwent in situ tensile testing. A Xeuss 2.0 diffractometer (Xenocs) operating at 50 kV and 60mA ($CuK\alpha_1$ radiation) and a 2D hybrid pixel camera detector (Dectris Pilatus 3R), was used. The sample-to-detector distance is 135.2mm, and the X-ray beam size is 0.8×0.8 mm^2. The angular range in 2θ varies from

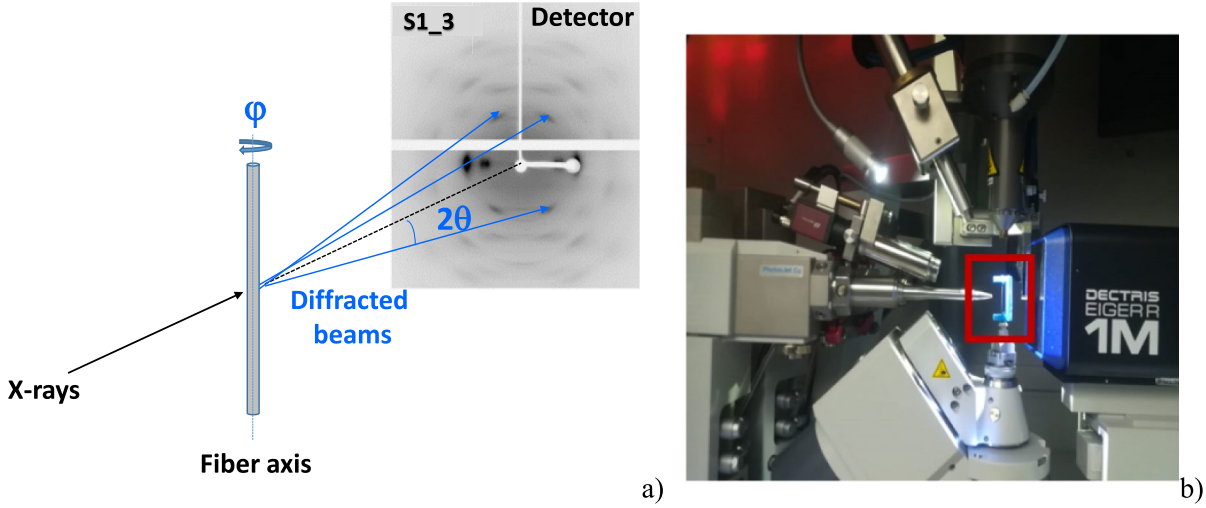

Fig. 1 **a** Diffraction geometry for the transmission experimental set-up. θ is the Bragg angle and φ the azimuthal angle in the diffractometer space. **b** Home-made 3D-printed sample holder (red rectangle)

0° to approximately 38° in this setup (Fig. 2b), with an acquisition time of 10 min per pattern. Measurements were conducted under primary vacuum.

Two different types of measurements were then carried out. Firstly, to characterize longitudinal variations in flax fibre ultrastructure, diffraction patterns were recorded at various points on a 50mm -long fibre bundle (sample S2_6). The sample was scanned at seven points along its longitudinal axis in 5mm steps (from 5mm to 35mm).

Secondly, starting from the undeformed state, the three samples S2_4, S2_5 and S2_7 were deformed from 0.2% to 0.6% or 1.2%, using 0.2% increments, the limit deformation values achieved just before sample ruptures (Table 3). For a given imposed strain value, stress relaxation is observed due to rearrangements of the polymeric chains of its ultrastructure.

Table 2 Summary of the 17 measurements performed on undeformed samples; square brackets (sample S2_6) after undeformed sample name indicate the longitudinal positions

	Serie 1				Serie 2						
Number of measurements	1	1	1	1	1	1	1	1	1	7	1
Sample name measured at a fiber longitudinal position of 15 mm	S1_1	S1_2	S1_3	S1_4	S2_1	S2_2	S2_3	S2_4	S2_5	S2_6	S2_7
S2_6 sample name also measured at 5 extra longitudinal positions	_									S2_6 [5 mm] S2_6 [10 mm] S2_6 [20 mm] S2_6 [25 mm] S2_6 [30 mm] S2_6 [35 mm]	_

Samples S2_4, S2_5 and S2_6 were then deformed to 0.2 up to 1.2% depending on the sample (Table 3)

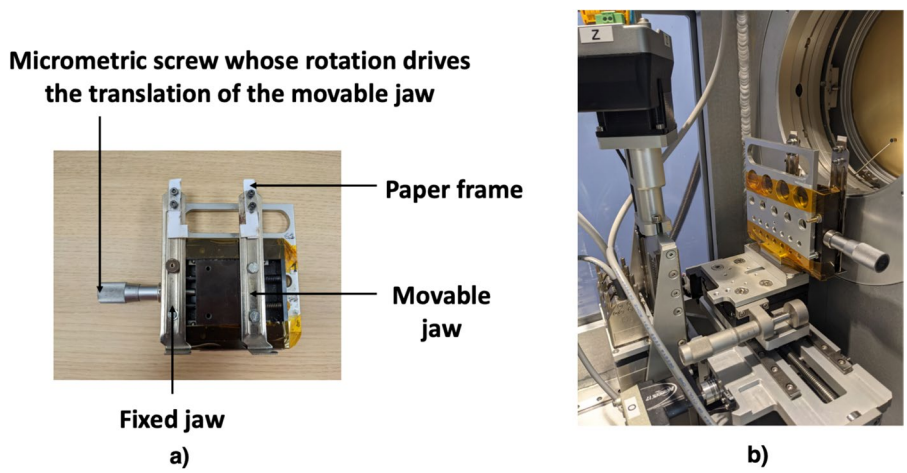

Fig. 2 **a** Micro-traction sample holder **b** Mounting of the sample holder on the diffractometer used for sample measurements

Table 3 Strain applied for X-ray diffraction measurements performed on samples S2_4, S2_5 and S2_6

Undeformed sample name	Deformed sample name with a given ε applied strain (%)						
	ε = 0.2%	ε = 0.4%	ε = 0.5%	ε = 0.6%	ε = 0.8%	ε = 1%	ε = 1.2%
S2_4	S2_4_0.2	S2_4_0.4	-	S2_4_0.6	S2_4_0.8	S2_4_1	S2_4_1.2
S2_5	S2_5_0.2	S2_5_0.4	-	S2_5_0.6	-		
S2_6	S2_6_0.2	-	S2_6_0.5		S2_6_0.8		S2_6_1.2

To minimize such rearrangements during diffraction pattern acquisition, it is crucial to know the stress stabilization time associated with the ultrastructure after loading. Our experience demonstrated that after each deformation step a stabilization time of 15 min is necessary (Gogoli et al. 2022.) before the pattern recording (Fig. 3).

In summary, we carried out 17 diffraction measurement sets on 11 different samples in the undeformed state. The 15 mm longitudinal position was measured on all samples while 6 additional longitudinal positions were measured on sample S2_6, at 5, 10, 20, 25, 30 and 35 mm along the flax fiber bundle.

The diffraction pattern analysis using the combined texture/structure/microstructure method allowed characterizing the main parameters accessible to X-ray diffraction (phases, crystallite sizes, texture, MFA). Instrumental contribution was accounted for using a polycrystalline standard sample assumed to be perfect within our instruments resolution (*i.e.* without defect, without microstrains, with large and isotropic crystallites) measured under the same experimental conditions (NAC ($Na_2Ca_3Al_2F_{14}$) and silver behenate ($C_{22}H_{43}AgO_2$) powders for Series 1 and 2 respectively). The main instrumental parameters that have been refined are 2D image center, sample-to-detector distance, diffraction peak broadening using a Caglioti function (Caglioti et al. 1958). These latter have then been kept constant during Rietveld analysis of our samples in MAUD.

Combined analysis structure/microstructure/texture method

The need for combined analysis

In order to determine the structure and microstructure of a sample, it is necessary to be able to compare intensities measured by X-ray diffraction with those calculated theoretically for a given instrument geometry. To achieve this, we need to establish a model, which considers the structure of phases, their

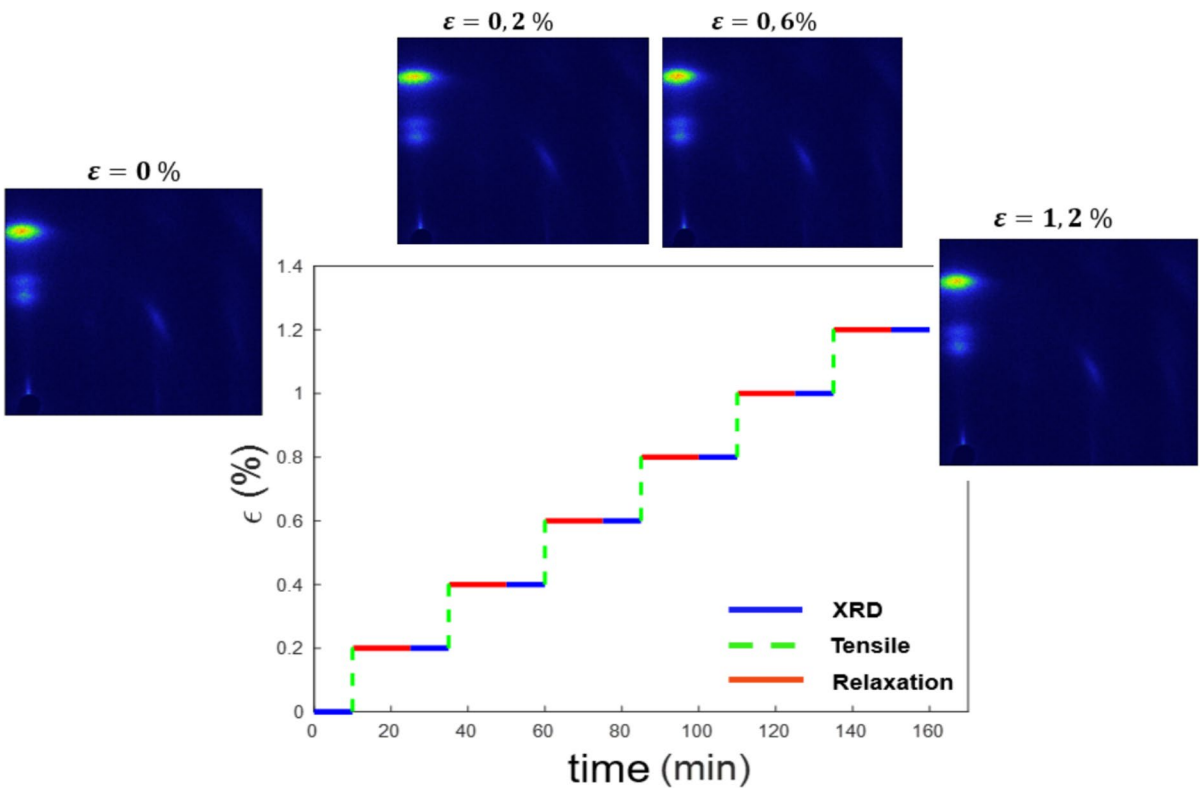

Fig. 3 Deformation chart applied to samples during diffraction experiments, with some 2D typical diffraction patterns (sample S2_4)

microstructure, and a given number of corrections (such as geometrical, absorption, Lorentz-polarization factor, scaling factor …) linked to the configuration of the measuring instrument. In the case of samples exhibiting crystallographic preferred orientations (texture), a Quantitative Texture Analysis (QTA) has to be operated to correctly model the observed intensities. QTA describes the orientation of all crystals' reference frames $K_c=(\vec{a},\vec{b},\vec{c})$, relative to the sample reference frame $K_A=(X_A, Y_A, Z_A)$ using a three-dimensional (3D) Orientation Distribution Function (ODF), refined from measured pole figures, 2D projections of the 3D ODF also called f(g). This latter is the probability density to find crystals having an orientation (g) within g and g+dg: $\frac{\Delta V(g)}{V}=f(g)dg$. After normalization, pole figures $P_{\vec{h}}(\vec{y})$ display the probability density of finding poles to (hkl) lattice planes (*i.e.* [hkl]* reciprocal directions) along specific $\vec{y}$ directions of the sample K_A frame. Integrating such pole figures over a solid angle $dy=sin\vartheta_y d\vartheta_y d\varphi_y$ gives the crystallites volume density oriented with $\vec{h}=<\mathbf{hkl}>^*$ normals between $\vec{y}$ and $\vec{y}+d\vec{y}$ (Fig. 4). Each pole figure point density is then used to correct the corresponding XRD pattern points.

Since both texture and structure contribute to the diffracted intensity measured for a given point of the 2D diffraction image, if the texture (ODF) is not perfectly known, information related to the structure can be biased, and vice versa. Therefore, both quantities need to be refined simultaneously within a global characterization methodology, known as "Combined Analysis", which operates QTA, structure and microstructure analyses. This technique, originally implemented in the MAUD (Materials Analysis Using Diffraction) software under the name "Rietveld-Texture analysis" (Lutterotti et al. 1997), is based on the Rietveld approach (Rietveld 1969), later extended to Combined Analysis (Chateigner et al. 2019) when incorporating residual stresses, layering, reflectivity analyses. It has been successfully used to obtain more detailed information on the texture and microstructure of cellulose, particularly in plant fibres (Driemeier 2014; Driemeier and Calligaris 2011; A. Thygesen et al. 2005). In MAUD, after extracting the integrated intensities in the first refinement cycle, the first ODF is refined based on an initial structure and microstructure model (Le Bail 2005). This first ODF is used in a second cycle to refine the structure and microstructure. This loop is then repeated until the solution converges to a best fit (Fig. 5).

Once the refinement has been carried out, the agreement between the calculated and the measured diffractograms must be checked. For this, several reliability factors can be used (Hill and Flack 1987).

Several models (Chateigner et al. 2019), including Standard Functions (Matthies et al. 1988), can be used to refine the ODF. This latter model is ideal for describing symmetrical enough textures, which is usually the case of polymeric materials exhibiting a preferred orientation around a principal axis (fibre texture), such as isotactic polypropylene (Lutterotti et al. 2007). According to the literature, in flax fibres, the crystalline direction ⟨001⟩ of the crystallites is aligned with the axis of the microfibrils, which is inclined by MFA with respect to the Z_A sample axis (Fig. 6a). This arrangement of crystallites suggests considering the <001> directions aligned on a cone of axis around each Z_A axis, with a cone aperture corresponding to the MFA of typically 5°-10° (Fig. 6b). For fiber bundles, as measured here, some misorientations between the fibrils are introduced, which overlap the 5° range. Consequently, a <001> fibre texture with the fibre axis aligned with fiber bundle Z-axis

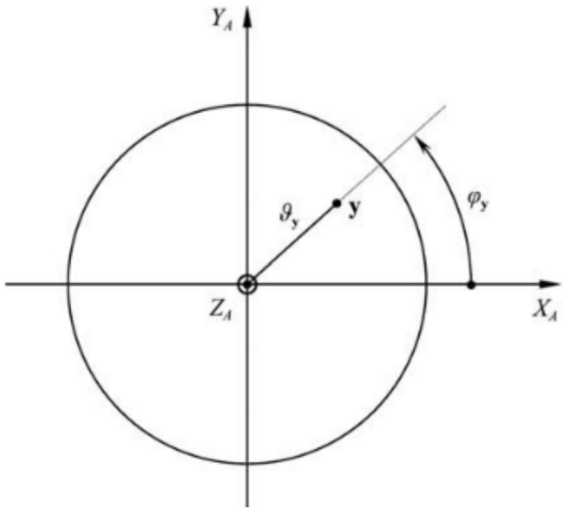

Fig. 4 $P_{\vec{h}}(\vec{y})$ pole figure for a crystallite with direction $\vec{y}$ (direction of the scattering vector in sample coordinate system, K_A frame) associated with the $\vec{h}$=[hkl]* vector

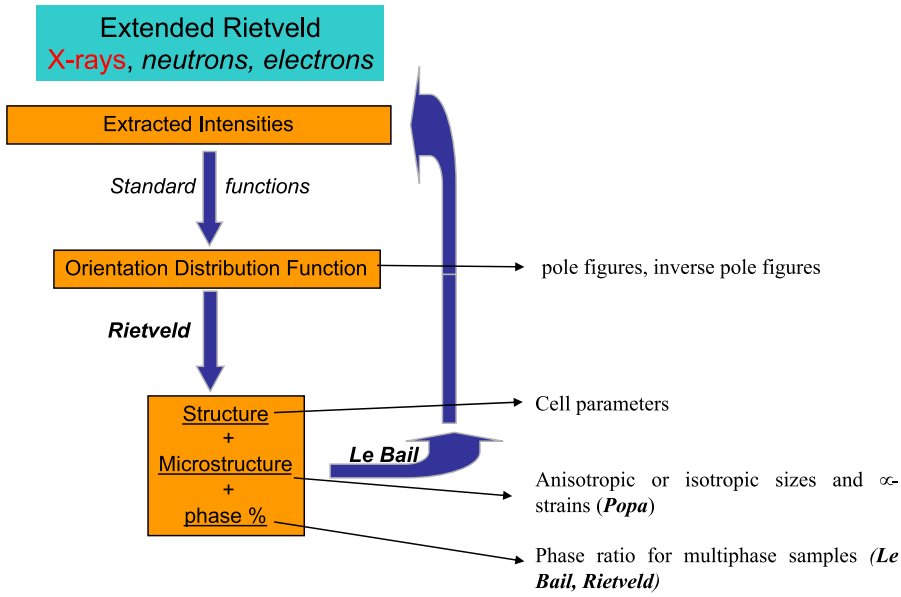

Fig. 5 Combined analysis loop for X-ray diffraction experiments

can be assumed (Fig. 6c) for the samples having a Iβ monoclinic cellulose structure (Table 1).

Moreover, the advantage of using a Rietveld-like approach lies in its capability to resolve peak overlaps (the case of cellulose), which, coupled with ODF refinement on standard functions, helps to obtain the true orientation distributions, using only few refinable parameters (profile widths and shape), hereby accelerating refinement calculations. We choose standard function model implemented in MAUD, which combines Gaussian and Lorentzian orientation components having a fibre symmetry. We then refined their mean position in orientation space, distribution width and the Gaussian–Lorentzian mixing parameter. The mean position of the fibre component is defined through 2 spherical angles of the pole figures, ϑ_y and φ_y (Fig. 4), and the h direction of the fiber is defined using two other spherical angles, ϑ_h and φ_h, with respect to c- and a-axes respectively. In our case the $<001>$ fibre texture can be modelled using all zero-values for these four angles.

Crystallographic considerations on crystal structure and refined parameters

According to (Duchemin et al. 2012; Oliveira and Driemeier 2013), refining the structure by considering only cellulose Iβ, though the major phase in plant fibres, gives rise to a couple of inaccuracies. In a first attempt, we however operated Rietveld refinements using only cellulose Iβ, and the crystallographic structure model proposed by Nishiyama et al. 2002. For all measurements, the spectrum backgrounds coming from incident X-rays scattering on air (Thomson scattering), was modelled using a second-order polynomial. It is worth noticing that this is not a "subtraction", as usually practiced when using "manual" analyses, but a convolution of the two contributions, background and crystalline cellulose phase. After several attempts using the previously described two contribution model, due to the semi-crystallinity of flax, the introduction of a second phase appeared necessary to account for broad signals neither belonging to the background contribution nor to Iβ. The nearly amorphous second phase was modelled using the approach of (Lutterotti 2012), aligned with that of (Le Bail 1995). In this approach the amorphous phase contribution to the diffraction signal is modelled using crystallite sizes close to lattice parameters. This second cellulose Iβ phase accounts for what is usually called "paracrystalline cellulose" that could also be named "nanocrystalline cellulose" according to our chosen approach. We introduced it in the model using isotropic crystallite sizes of an ad hoc mean size, to encompass the non-fully crystallized part of the flax. However, for the crystalline Iβ cellulose, it has been necessary

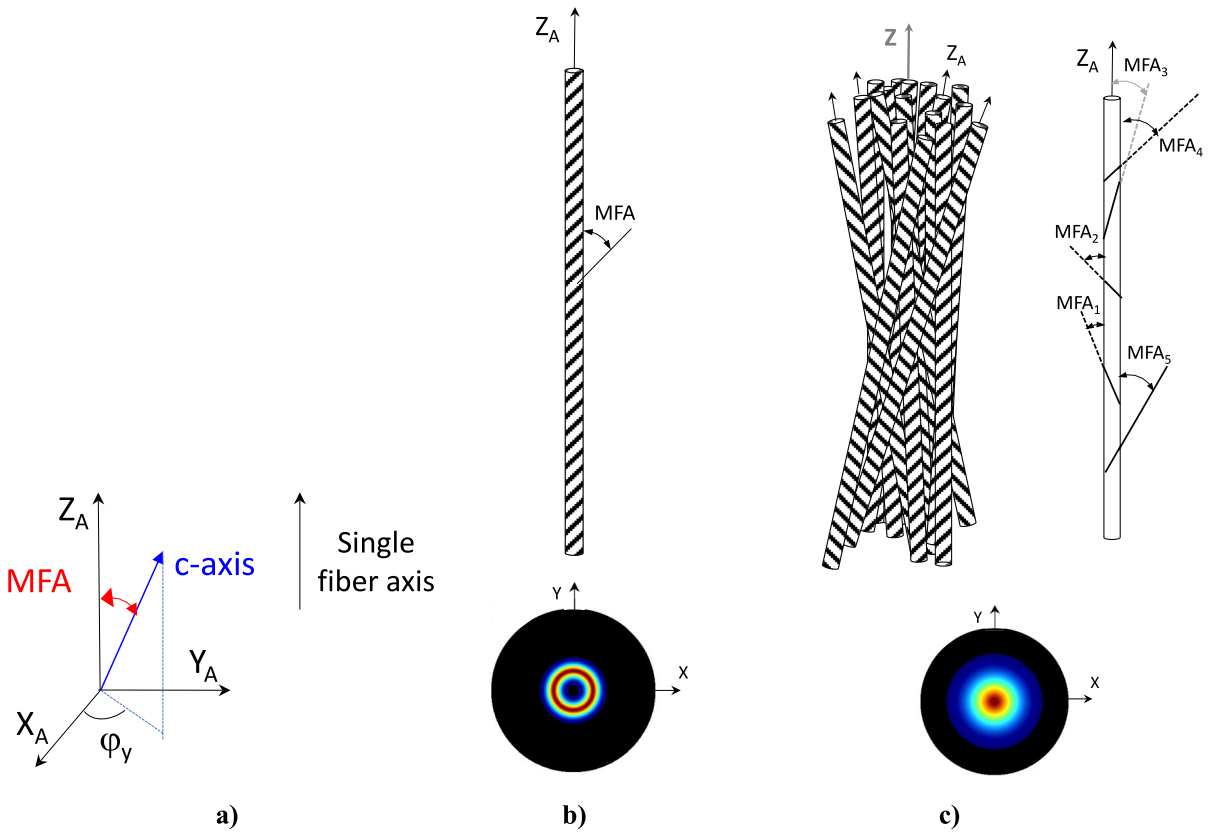

Fig. 6 **a** Schematic microfibril angle (MFA) for a Z_A axis single fiber **b** Representation of cellulose microfibrils inclined of one MFA value with respect to the Z_A-axis of a flax elementary fibre and its corresponding simulated non centered {001} pole figure **c** Disorientation representation of several previous elementary fibres along the Z-axis of a flax bundle (left) and representation of cellulose microfibrils inclined of various MFA value with respect to the Z_A-axis of a flax elementary fibre (right) resulting in the same simulated centered {001} pole figure. MFA value of 0° or 90° corresponds to a ϑ_y angle (Fig. 4) of 0° or 90° in the pole figure

to introduce anisotropic crystallite sizes using the Popa approach (Popa 1992, 1998). In this approach the calculation of the average size $< R_{\vec{h}} >$ of crystallites in the $\vec{h}$ crystal direction is determined by performing its development into symmetrized spherical harmonics series, the coefficients of which being refinable parameters satisfying the Laue groups. In our samples, no Gaussian contribution to the peak broadening along 2θ could be detected, indicating the absence of significant microstrains.

Then, in all refinements, the parameters refined in the MAUD software are: second order polynomial background parameters, lattice parameters a, b, c and γ (cellulose monoclinic Iβ for the crystalline and nanocrystalline phases), anisotropic crystallite sizes for the crystalline phase and isotropic crystallite size for the paracrystalline (nanocrystalline) phase, parameters of the Standard Function model used to extract the $< 001 >$ fibre texture. For in situ deformation measurements, we successfully could refine the phase fractions, while the strong fluorescence signal from the beam stop prevented this determination for the other measurements.

Reliability factors are given to evaluate the quality of the refinement, for both the overall Rietveld refinement of the whole set of diffraction data and the ODF refinement from experimental pole density values. We use R_w weighted R-factors (Hill and Flack 1987). However, the quality of the fit is first systematically checked by visually comparing measured and

calculated 2D patterns. Indeed, as discussed by Toby et al. (2006), the 2D representation is more reliable to assess the global quality of fit, including texture. The overall texture strength is given using the texture index $F^2 = \frac{1}{8\pi^2}\sum f(g)^2\, dg$ (Chateigner 2005).

Results and discussions

In order to perform Combined Analysis, the measured diffraction patterns (Fig. 7a) must be converted into diffractograms $(2\theta, I(2\theta))$ (Fig. 7b and c). The 2D diffraction images are integrated and converted into MAUD, resulting in 65 or 179 diagrams (depending on the diffractometer and detector), each one corresponding to an azimuthal slice, η, of 2° in the range $0° < \eta < 360°$ (Fig. 7a). The formulas for converting from 2D space (diffraction pattern) to diffractograms $(2\theta, I(2\theta))$ are detailed in (Lutterotti et al. 2014).

All blind areas on detectors (detector interspace, beam stops, beam stop holders …) are removed from the analyses (Fig. 7a).

Whatever the samples, refinement results (Figs. 8 and 9) confirm the effectiveness of the two-phase model in reproducing the experimental spectra of cellulose, with reasonably low R_{wp} factors values indicating that both structural and textural models can satisfactorily describe the samples (Table 5). They clearly highlight the respective contributions of crystalline and paracrystalline phases (Fig. 8). The crystalline phase exhibits sharp diffraction peaks, while the paracrystalline phase, characterized by a less pronounced organization of cellulose chains, shows much broader peaks. In Fig. 8, black arrows indicate the five main diffraction peaks of crystalline cellulose Iβ. However, the full list of peaks (black vertical lines of Fig. 8 bottom) reveals many other low-intensity peaks, strongly overlapped due to the low crystalline symmetry of cellulose. Also noteworthy is a significant difference in the position of peaks corresponding to the two types of cellulose (crystalline and paracrystalline phases used in our Rietveld refinement).

The strong diffracted intensity variations with η on the experimental diagrams (Fig. 9a, bottom) clearly shows the strong texture of the crystalline Iβ phase and the good reproduction of this texture on the simulated diagrams (Fig. 9a, top). Low residuals between experimental and simulated data are accomplished (Fig. 9b). The texture strengths F^2 are typically ranging from 10 to 20 mrd^2 in our samples, indicating a rather strong texture.

Structure, microstructure and texture of crystalline cellulose Iβ

Structure of cellulose Iβ

Discussion of Series 2 results The crystalline phase of the undeformed samples (Table 2), exhibits different refined crystal lattice parameters compared to the initial cellulose parameters from Nishiyama et al. 2002. The a and b refined parameters are on an average larger than those of (Nishiyama et al. 2002), which are 7.784 and 8.201 Å respectively (Table 1), while the mean c parameter *c* is lower than the initial value of 10.38 Å. The refined γ angle with a mean value at 97.33° is also larger than 96.5° (Table 4). The standard deviations (sd) on the mean values show that there are more variations of the cell parameters between samples than along a given sample of restricted length (S2_6). It should be emphasized that the crystal structure of cellulose Iβ, used as the starting structure, was solved from tunicin (Nishiyama et al. 2002), a form of cellulose made by marine animals. Even if, to date, this structure model is the best available approximation to the crystal structure of cellulose Iβ one might expect slight deviations for plants' cellulose.

For sample S2_6, for which several volumes were probed along the longitudinal fiber axis (Table 4), the refined b and γ values exhibit larger standard deviations compared to a and c values. The coherent size domains (crystallite sizes) are larger along c- compared to a- and b-directions. It consequently seems that cellulose growing is accompanied by more regular structural stabilization.

The volume fraction of the Iβ crystalline phase, χ_v, varies between 53 and 65% (Table 4) with a mean value at 61%. Such values correspond to a refined mass crystallinity between 64 and 69%, in line with flax crystallinity degrees reported in the literature (Fink et al. 1999; Lennholm et al. 1994). It is also evidenced for sample S2_6 (bundle of 50 mm long fibres), that for the different longitudinal positions, within standard deviations, the crystallinity degree can be considered as constant, with a χ_v value around 61% (Table 4).

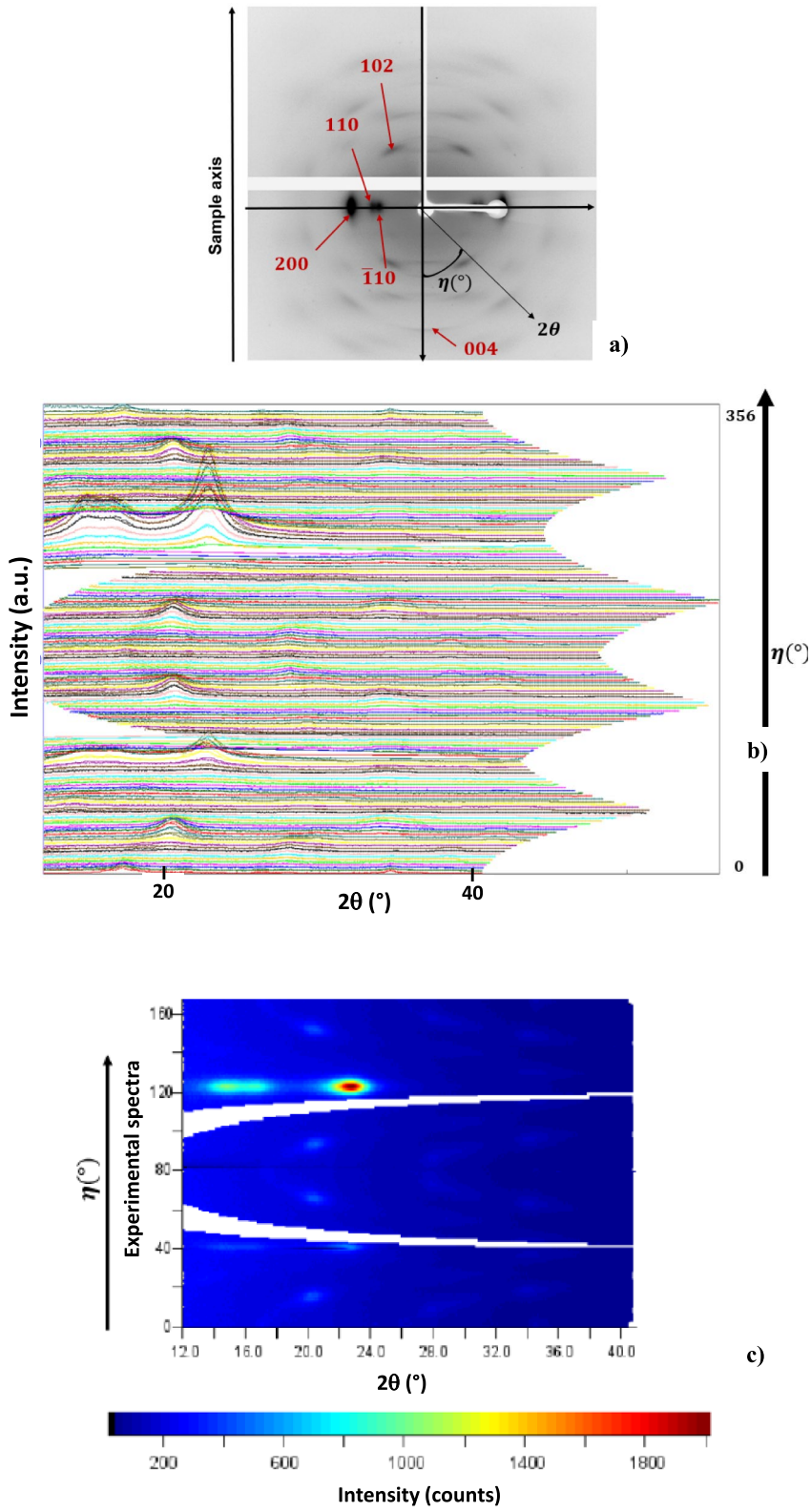

Fig. 7 **a** 2D-diffraction image of a microfibril bunch using the Eiger detector of the Rigaku diffractometer, illustrating the strong cellulose fibre texture **b** Illustration of the η azimuthal slice conversion of image into diffractograms (2θ, I(2θ)) with 2θ the scattering angle **c** corresponding 2D plot with 179 diffractograms

Table 4 Refined lattice parameters (a,b,c,γ), anisotropic crystallite sizes (D_{100}, D_{010}, D_{001}), and volume fraction (χ_v) of the crystalline phase of undeformed samples. For sample S2_6, we measured spectra at different longitudinal positions along the flax fiber bundle: square brackets after undeformed sample name indicate these longitudinal positions Parentheses are standard deviations on the last digit given as 1σ from the refinement

Crystalline phase Iβ								
Undeformed samples	a(Å)	b(Å)	c(Å)	γ(°)	D_{100} (nm)	D_{010} (nm)	D_{001} (nm)	χ_v (%)
S2_1	8.24 (1)	9.05 (3)	10.28 (2)	97.55 (6)	14.78 (4)	14.78 (4)	22.24 (3)	53 (2)
S2_2	8.23 (1)	9.09 (3)	10.15 (2)	97.65 (7)	12.49 (5)	12.49 (5)	21.86 (6)	54 (2)
S2_3	8.24 (2)	9.00 (3)	10.25 (3)	97.47 (7)	13.79 (1)	13.79 (1)	18.94 (3)	59 (3)
S2_4	7.96 (1)	8.35 (2)	10.37 (1)	97.29 (5)	14.74 (4)	14.74 (4)	20.80 (2)	64 (1)
S2_5	8.06 (2)	8.51 (5)	10.36 (3)	97.44 (1)	13.94 (1)	13.94 (1)	22.95 (6)	61 (5)
S2_6 [5 mm]	7.95 (1)	8.37 (3)	10.36 (1)	97.38 (6)	14.74 (5)	14.74 (5)	20.80 (4)	64 (3)
S2_6 [10 mm]	8.04 (2)	8.52 (3)	10.4 (2)	97.27 (7)	16.11 (3)	16.11 (3)	21.96 (3)	62 (2)
S2_6 [15 mm]	7.88 (1)	8.17 (3)	10.3 (2)	97.24 (7)	20.99 (3)	20.99 (3)	29.85 (5)	60 (2)
S2_6 [20 mm]	7.94 (1)	8.22 (3)	10.25 (2)	97.19 (7)	19.81 (4)	19.81 (4)	31.50 (2)	62 (2)
S2_6 [25 mm]	7.888 (8)	8.21 (2)	10.25 (1)	97.02 (5)	22.57 (3)	22.57 (3)	35.17 (2)	60 (2)
S2_6 [30 mm]	7.94 (2)	8.23 (3)	10.25 (2)	97.17 (8)	18.33 (6)	18.33 (6)	35.74 (4)	61 (3)
S2_6 [35 mm]	7.890 (9)	8.23 (2)	10.27 (1)	97.2 (1)	20.02 (4)	20.02 (4)	36.38 (2)	62 (2)
S2_7	8.00 (2)	8.45 (4)	10.43 (2)	97.42 (7)	17.13 (1)	17.13 (1)	25.35 (2)	65 (3)
Overall mean	8.02	8.49	10.30	97.33	17	17	26	61
Overall sd	0.13	0.34	0.08	0.17	3	3	6	4
S2_6 mean	7.93	8.28	10.30	97.21	19	19	30	62
S2_6 sd	0.06	0.12	0.06	0.11	3	3	6	1

D_{100} and D_{010} are strictly equal in these refinements since the series expansion was limited to a cylindrically symmetric shape model. The last four lines are overall means values and mean values for sample S2_6 with their respective standard deviations (sd)

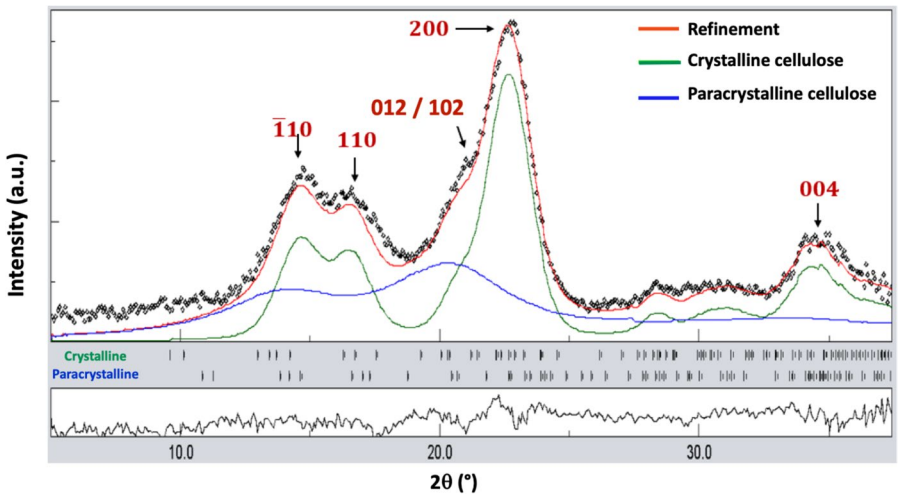

Fig. 8 Example of a Rietveld refinement of 65 summed diffractograms (black dots) of cellulose from an undeformed S2_5 sample. The contribution of both phases to the overall spectrum (red) is highlighted (green: crystalline phase; blue: "paracrystalline" phase). For each phase, black vertical lines mark the positions of the various diffraction peaks. The lower rectangle shows the difference diagram between the summed experimental diffractogram and the refined one

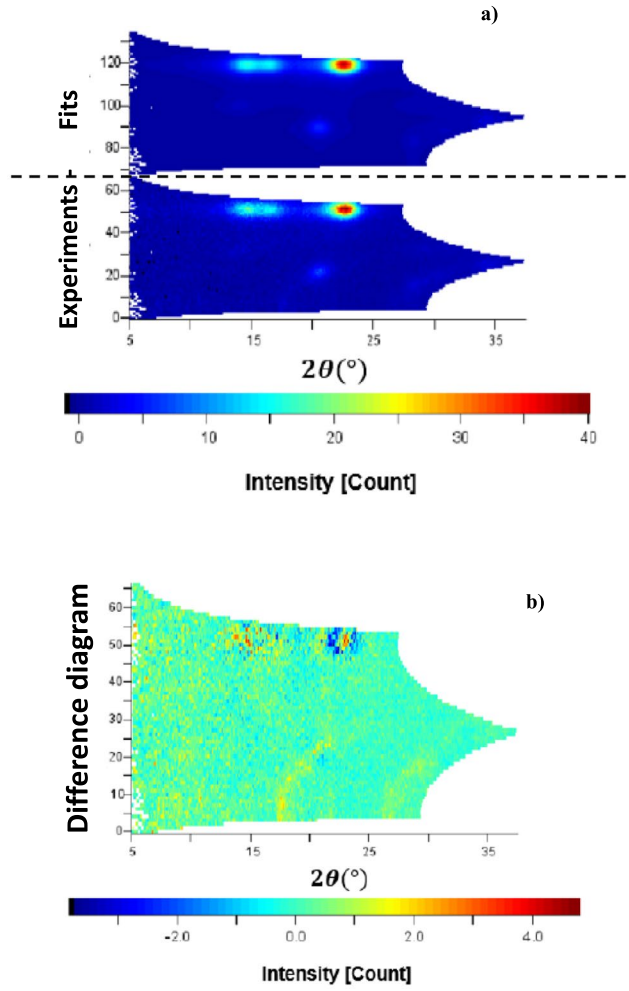

Fig. 9 Example of **a** 2D experimental (bottom) and refined (top) diagrams as extracted by MAUD from diffraction images of a flax fibre bunch **b** Difference between experimental and refined diagram showing the very good agreement between the experimental model and the one used to refine the 65 spectra of the S2_5 sample

Table 5 Refined lattice parameters (a, b, c, γ), anisotropic crystallite sizes (D_{100}, D_{010}, D_{001}) and F^2 texture index values of the crystalline phase of Series 1 undeformed samples with their corresponding R_{wp} factors

Crystalline phase, Series 1 undeformed samples									
Samples	a(Å)	b(Å)	c(Å)	γ(°)	D_{100} (nm)	D_{010} (nm)	D_{001} (nm)	F^2 (m.r.d.^{2})	R_{wp} (%)
S1_1	7.873 (1)	8.301 (3)	10.351 (1)	96.560 (1)	7.95 (4)	4.24 (5)	9.50 (1)	8.7	6.59
S1_2	7.886 (2)	8.281 (2)	10.380 (5)	96.73 (3)	9.95 (2)	5.21 (3)	12.08 (4)	26.4	7.73
S1_3	7.873 (1)	8.301 (3)	10.351 (9)	96.550 (1)	6.98 (3)	2.28 (2)	8.36 (5)	14.1	7.98
S1_4	7.874 (8)	8.301 (1)	10.351 (8)	96.549 (8)	5.04 (3)	0.42 (4)	7.43 (2)	20.9	12.53
Mean values	7.876	8.296	10.358	96.599	7.5	3.0	9.3		
Sd values	0.006	0.01	0.014	0.087	2.0	2.1	2.0		

Parentheses are standard deviations on the last digit for 1σ as given by MAUD. D_{100} and D_{010} have different values in these refinements since the series expansion was not limited to a cylindrically symmetric shape model. The last two lines are overall mean values and the respective standard deviations for the refined cell parameters and anisotropic crystallite size values

Discussion of series 1 results The covered measurement angular range in 2θ for Series 1 (0 to 55°) is larger than the one for Series 2 (0 to 38°). Consequently, for Series 1, taking into account the refinement of the paracrystalline phase led to inconsistent results. Since the signal from the paracrystalline phase is weaker than that from the crystalline phase, it is likely to be more affected by the parasitic fluorescence signal from the diffractometer's double beam stops. Therefore, lattice parameters of the paracrystalline phase were fixed to the values of (Nishiyama et al. 2002) without significant impact on the physical meaning of the refinement, especially of texture. Good agreement was then obtained between the calculated and measured 179 spectra (Fig. 10) and as asserted by the obtained reliability factors (Table 5).

As evidenced for Series 2, the refined cell parameters for the crystalline phase of Series 1 (Table 5) are different from, but closer to, those of (Nishiyama et al. 2002). Between samples S1_1, S1_3 and S1_4, the refined lattice parameters are equal within the standard deviations. Interestingly, thanks to the larger 2θ span for Series 1, the smaller mean standard deviation confirms that flax fibres of our work exhibit different unit-cell parameters compared to Nishiyama et al. 2002 work.

Microstructure of undeformed samples: crystallite shapes and sizes

Taking into account the anisotropic distribution of crystallite dimensions during refinements using the Popa approach (Popa 1992, 1998), we can access the

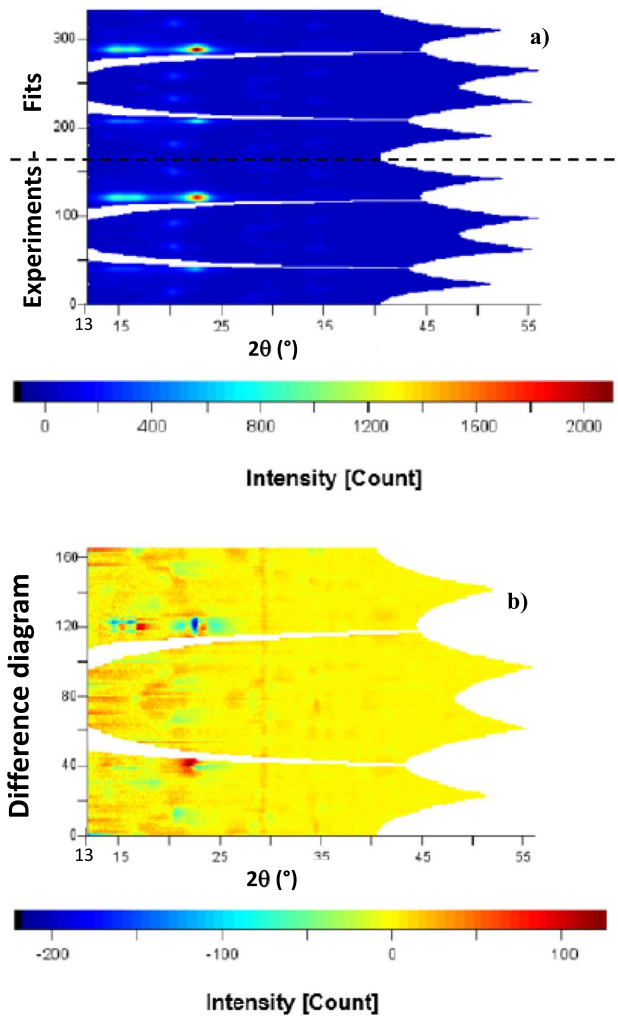

Fig. 10 **a** Experimental (bottom) and refined (top) 2D spectra of Series 1 sample S1_2 **b** Difference between experimental and refined diagram showing the very good agreement between the experimental model and the one used to refine the 179 spectra of the S1_2 sample

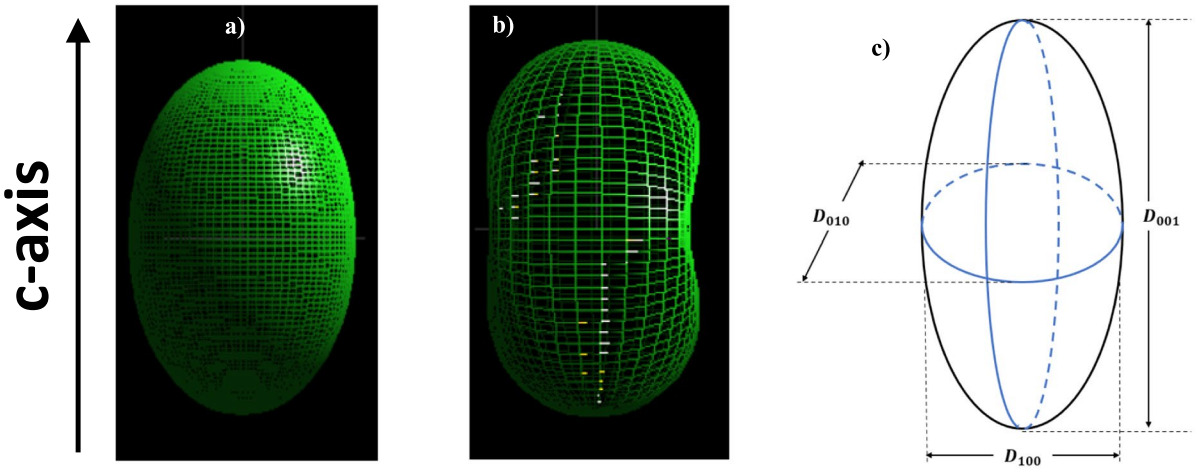

Fig. 11 MAUD 3D reconstruction of flax crystallite shapes for respectively series 2 and series 1 samples exhibiting **a** cylindrically and **b** non-cylindrically refined symmetric shape model and **c** their corresponding schematic

Table 6 Summary of crystalline cellulose crystallite minimum and maximum dimensions found by the combined analysis applied on N = 17 samples

Series 1			
$N=4$	$D_{100}\,(nm)$	D_{010}(nm)	D_{001}(nm)
Min	5.04	0.42	7.43
Max	9.95	5.21	12.08
Series 2			
$N=13$	$D_{100}\,(nm)$	$D_{010}(nm)$	$D_{001}\,(nm)$
Min	12.49	12.49	18.94
Max	22.57	22.57	36.38

average sizes of crystallites for main crystal directions. This leads to the three-dimensional reconstruction of crystallites (Fig. 11**),** showing that the crystallites in the flax crystalline phase are modelled as elongated ellipsoids, with their $\vec{c}$ axes along the long axis of the ellipsoid. These crystallites longitudinally assemble into chains to form microfibrils that twist helically around the sample axis. It has been demonstrated that, depending on the cellulose source, the cross-section of crystallites can be hexagonal (Bayer et al. 1998; Duchemin et al. 2012; Newman et al 2013), rhombohedral (Bu et al. 2015; Lehtiö et al. 2003; Oehme et al. 2015), elliptical (Ding et al. 2014; Ding and Himmel 2006; Leppänen et al. 2009), or rectangular (Oehme et al. 2015; Thomas et al. 2013). According to our analysis, the cross-section of flax crystallites is elliptical or quasi-elliptical in the equatorial bulging regions (Fig. 11). Considering both sets of measurements (Table 6), the crystallites have an average cross-section around 15*nm* in the ⟨100⟩ direction and a width of 14*nm* in the ⟨010⟩ direction. Although the diameter of microfibrils can vary from 2 to 20*nm* depending on their origin (Hamad and Hu 2010), the dimensions derived from our Rietveld analysis are on an average larger than the widths of flax crystallites reported in the literature (Duchemin et al. 2012; Leppänen et al. 2009; Müller et al. 2004; Viljanen et al. 2022). The differences observed can be explained by the fact that in many X-ray diffraction studies, the Scherrer equation is used, which generally obtain an apparent crystallite size in the ⟨100⟩ direction based on isotropic (spherically shaped) crystallite sizes. This approach does not take into account possible peak overlaps, such as the 012/102 peak embedded in the flank of the 200 peak (Fig. 8), in these low-symmetry structures. Even if in the work of Viljanen et al. (Viljanen et al. 2022), the authors separate these two contributions, it has been made with no diffraction intensity constraint, using Gaussian line profiles, on a single integrated (along the Debye rings) diagram, in transmission geometry. Indeed, it is widely admitted in the literature (Popa 1992, 1998; Balzar et al. 2004) that peak broadening due to limited crystallite sizes provides width line profiles which are Lorentzian-like (if no other effects are visible) and that the Scherrer formula is restricted

to so-called symmetrical arrangement measurements, which is not the case for transmission setup. Moreover, the used Scherrer formula (with only one K factor) cannot estimate anisotropic crystal shapes and one has to remember that in transmission with cyclic-fibre textures the 200 and 012/102 (and other hkl lines) arcs cannot be exactly in Bragg position altogether. Combined analysis, on the other hand, makes it possible to refine widths in several directions after deconvolution of the contributions of each family of diffracting planes. Other works, such as those by (Ling et al. 2019), have also reported cotton crystallite sizes calculated by Rietveld analysis (MAUD) to be greater than those determined using the Scherrer equation. The latter does not take into account peak broadening due to microstrain and paracrystallinity (Hosemann and Hindeleh 1995; Kulshreshtha et al. 1969), leading to a possible underestimation of crystallite size.

Compared to Series 1 samples exhibiting smaller a- and b- cell parameters, the refined anisotropic crystallite sizes are larger in Series 2 (Table 6). Using both series, the average crystallite length, estimated from D_{001} widths, is around 23nm, compared with 17.8nm according to (Leppänen et al. 2009) for flax. Compared with other plant fibres, wood (*Picea abies*) has a crystallite length of around 30*nm* (Andersson et al. 2003; Oliveira and Driemeier 2013), cotton 25.6nm (Oliveira and Driemeier 2013), and microcrystalline cellulose displays lengths between 10 and 32.3nm (Duchemin 2017). Overall, D_{100} crystallite widths and D_{001} lengths generate an anisotropy factor (length/width) of the coherent domains between 1.2 and 2.

Effect of the tensile test on structural and microstructural properties

The analysis of the cell parameters and anisotropic sizes of the microfibrils showed no significant evolutionary trend under tension that could confirm, as (Placet et al. 2011a), that fibre tensile stress is accompanied by longitudinal extension of the cellulose crystallites along the ⟨001⟩ directions. In our opinion, further measurements and in-depth analyses on a larger number of fibres are essential in order to gain a broader and more accurate view of the evolution under tension of the microstructure and structure of flax fibres. One should also bear in mind that the imposed strains in our work are not larger than 1.2%, which probably does not give rise to large rearrangements of microfibrils. In non-biogenic polymers like Polypropylene, deformation-induced crystal size increase comes from polymer chains reorientations from the amorphous or poorly crystalline phases.

In our samples, no significant change in crystallinity during tensile testing was observed in any of our tests. In view of these results, the hypothesis of stress induced-crystallization of plant fibre cellulose cannot be confirmed by our work. However, the experimental conditions under which the Series 2 measurement were carried out could disfavour the paracrystalline cellulose crystallization. Indeed, some works (Roig 2011) show that amorphous cellulose can crystallize at room temperature when the water content reaches values of the order of 8%, due in particular to the drop in glass transition temperature caused by hydration (glass transition plasticization phenomenon). However, the Series 2 X-ray diffraction measurements were carried out under a primary vacuum—a pressure well below atmospheric pressure—which has the effect of affecting the water content of the sample. The environmental conditions that could favour the crystallization of flax paracrystalline or non-crystalline cellulose are therefore not fully met. In our future work, we will carry out diffraction measurements in a controlled environment to clarify the hypothesis of induced crystallization of plant fibres under the effect of mechanical loading.

Texture and MFA angles of the crystalline cellulose in undeformed and deformed samples

We must remember that QTA in our study has been operated for the crystalline orientation of a bundle of flax fibres, probing all the S_1, S_2 and S_3 layers of the secondary wall, which contains the majority of flax cellulose. However, given that the S_2 layer is significantly thicker (in terms of the thickness of the elementary fibre), the obtained results mainly reflect the arrangement of crystallites in this S_2 layer. For the crystalline phase, the standard function fibre model converged to a distribution of crystallites c-axes around the sample longitudinal axis, Z, with 90% of Gaussian character whatever the sample. This typical $<001>$ fibre-texture, explainable by the helical arrangement of the cellulose microfibrils, is visible on the {001} pole figure (Fig. 12a) exhibiting a

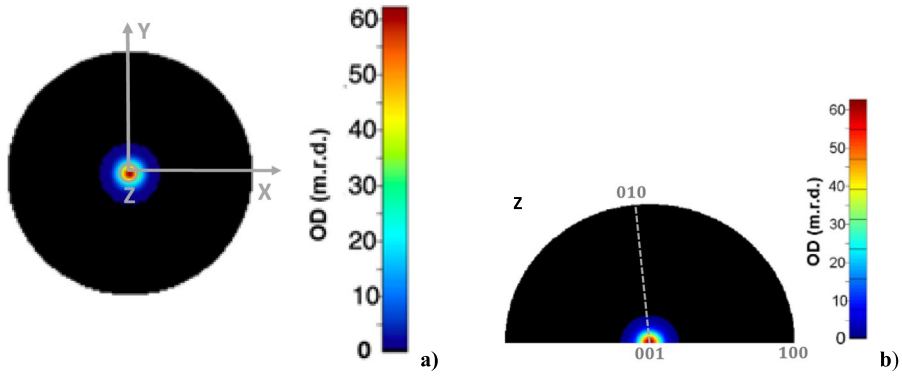

Fig. 12 Example of **a** {001} reconstructed normalized pole figure and **b** its corresponding Z-axis inverse pole figure. Equal area projections

strong reinforcement for its Z-axis. The inverse pole figure drawn for the Z-axis of the sample (Fig. 12b) only shows a [001] reinforcement, indicating that the < 001 > fibre is the only one component of orientation in the samples. Lets remark here that neither the shape of the distribution (Gaussian, Lorentzian or mix) nor its sharpness (or maximum) can be represented using a March Dollase-type correction, as used for instance by Duchemin et al. (2017). Indeed, the March Dollase correction, as it is defined (Chateigner et al. 2019), is not suitable for describing an orientation density distribution. This could explain why Duchemin et al. (2017) were obliged during Rietveld refinements to introduce another allomorph of cellulose. For the eleven samples, the Iβ cellulose exhibits high maximum orientation density values ranging from 40 to 100 m.r.d (1 m.r.d. i.e. 1 multiple of a random distribution, corresponds to a perfectly randomly oriented powder; in a single crystal the pole figures exhibit 0 m.r.d. values except for the exact crystal directions for which they tend to infinity). Such orientation levels correspond to large overall texture strengths, as depicted by the F^2 texture index values between 8.7 and 26.4 m.r.d.^{2} (Table 5).

As each cellulose microfibril is a chain of crystallites bound by amorphous domains, the observed inclination of the $\vec{c}$ axis then can correspond to the inclination of the microfibrils *i.e.* to the MFA (Fig. 6 a). Consequently, from the comparison between Fig. 12b and Fig. 6, the MFA values can be determined from the Z-axis of the {001} pole figure that give the cellulose crystallites c-axes orientation distribution with respect to the fibre bundle Z axis. The potential MFA values range from 0° at the centre of Fig. 12a, while its equator is at MFA = 90°.

From the pole figure data it becomes possible to calculate the distribution of MFA in flax fibre using the orientation density (OD) values of $P_{\vec{h}}(\vec{y})$ extracted from the MAUD software (Eq. 1) with here, $\vec{h} = \langle 001 \rangle$, the axis of the fibre texture. The volume fraction of crystallites oriented between $MFA = \vartheta_i$ and $MFA = \vartheta_f$ is obtained from the integral over the pole figure sphere (Eq. 1) for the corresponding MFA range, normed to the whole pole sphere. Since the obtained texture is of fibre type, *i.e.* for a given polar angle ϑ_y (Fig. 4), the OD on pole figures is independent of the azimuthal angle φ_y, the volume fraction simplifies to Eq. 2.

$$T_{\vartheta_i-\vartheta_f} = 100 \int_{\varphi_y=0}^{2\pi} \int_{\vartheta_i}^{\vartheta_f} P_{\vec{h}}(\varphi_y, \vartheta_y) \sin\vartheta_y d\vartheta_y d\varphi_y \Big/ \int_{\varphi_y=0}^{2\pi} \int_{\vartheta_y=0}^{\pi/2} P_{\vec{h}}(\varphi_y, \vartheta_y) \sin\vartheta_y d\vartheta_y d\varphi_y \quad (1)$$

$$T_{\vartheta_i-\vartheta_f} = 100 \frac{\int_{\vartheta_i}^{\vartheta_f} P_{\vec{h}}(\vartheta_y) sin\vartheta_y d\vartheta_y}{\int_{\vartheta_y=0}^{\vartheta_y=\pi/2} P_{\vec{h}}(\vartheta_y) sin\vartheta_y d\vartheta_y} \quad (2)$$

The values of $P_{\vec{h}}(\vec{y})$ were exported using a constant discretized step size of 5° in ϑ_y between 0° and 90°, resulting in nineteen values. Then, noting OD_i as the density $P_{\vec{h}}(\vartheta_{ci})$ corresponding to the center ϑ_{ci} of each interval $[\vartheta_i, \vartheta_{i+1}]$ $(i = 1, 2, ..., 18)$, the volumic fraction of microfibrils within $[\vartheta_i, \vartheta_{i+1}]$ can be calculated as (Eq. 3):

$$T_{\vartheta_i-\vartheta_{i+1}} = 100 \frac{OD_i \times sin\vartheta_{ci}}{\sum_k^{18} OD_k \times sin\vartheta_{c_k}} \quad (3)$$

We represent this volumic fraction as MFA histograms for all undeformed and deformed samples.

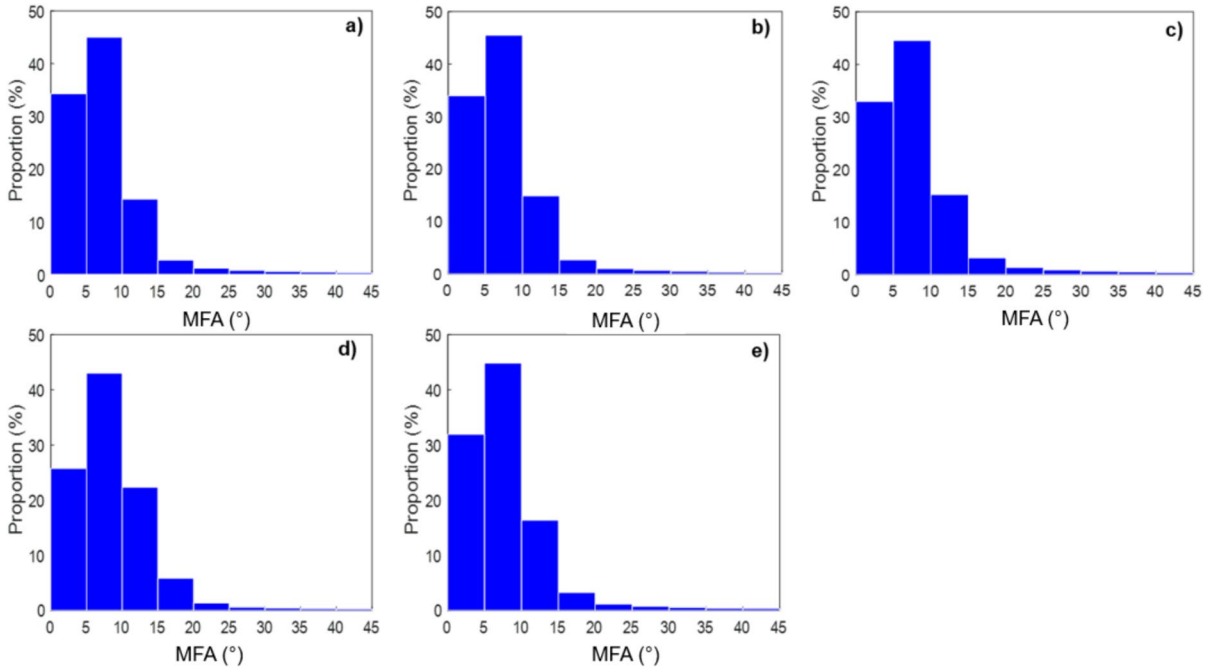

Fig. 13 MFA distribution histograms for undeformed samples **a** S2_1 **b** S2_2 **c** S2_3 **d** S1_1 **e** S1_3

MFA distribution in undeformed samples of Series 2

Figure 13 shows that around 90% of the sample volume corresponds to MFA values below 15°, with MFA never exceeding 45°. Depending on the sample, the volume fraction of microfibrils with MFA in the range 0–5° is within the 25 to 35% interval. Around 45% of the volume exhibits MFAs between 5 and 10°, while between 10 and 15°, this fraction goes to 13–20%, then drops to negligible values for larger MFA values. If contributions larger than 30° could be assigned to S_1 and S_3 crystalline contributions of the fiber layers (Roland et al. 1995), as the measured volume percentage evidenced for these contributions are smaller than 2%, we can conclude in our study that the MFA main contribution is mainly related to the S_2 layer. The large majority of MFA from crystalline regions is thus within the range of 0 to 20°, with a peak distribution between 5 and 10° FWHM, and it becomes interesting to get a look at variations within this distribution. One can note from these measurements that a decrease in the 10–15° volume fraction is accompanied with an increase between 0 and 5°, while the fraction of microfibrils between 5 and 10° remains relatively stable around 45%. Considering all measurements, above 20°, the values become very low and virtually negligible. It should be noted that the MFA distribution of flax fibre derived in this work from Combined Analysis is similar to the one of elementary flax fibres found by second harmonic generation microscope observations, which revealed heterogeneous MFA distributed along the elementary fibre, predominantly between 0 and 10°, with an average value around 5° (Melelli et al. 2020a, b). The MFA distributions observed in our samples are then rather due to the intrinsic MFA distributions of elementary fibres than to distributions introduced when shaping the bundles for measurements. Also, the histograms constructed in this work show an average MFA lying between 5 and 10°, we are confident in comparing our results derived from Rietveld's analysis with other published data (Table 7).

The range of average MFA values is in agreement with the ones found by Bourmaud et al. (2013), Wang et al. (2020), and, to a lesser extent, those of Viljanen et al. (2022) and Melelli et al. (2020a, b a). In the MAUD software, using a sharper discretization of the ODF would probably be desirable to be able to access to finer comparison with the microscopy work of Melelli et al. (2020a, b a).

Table 7 Comparison of the average MFA of flax fibre bundles determined by different studies

Type of sample	Method	Mean MFA	Reference
Fibre bundle	XRD, combined analysis	5°-10°	This study
Fibre bundle	XRD, azimuthal profile of peak (200)	8°-12°	(Viljanen et al. 2022)
Elementary fibre	Second harmonic generation microscopy	5°	(Melelli et al. 2020a, b a)
Fibre bundle	XRD, azimuthal profile of peak (200)	6.2°-7.2°	(Wang et al. 2020)
Fibre bundle	SEM observations	5.8°-7°	(Wang et al 2020)
Fibre bundle	XRD, azimuthal profile of peak (200)	8.3°-9.5°	(Bourmaud et al. 2013)
Fibre bundle	SAXS	5.5° (dry sample) - 7.5° (wet sample)	(Astley & Donald 2001)
Elementary fibre	SAXS	4.7° – 7.4°	(Richely et al. 2022)
Elementary fibre	SAXS	3.5°-6.4°	(Müller et al. 2000; Muller et al. 1998)

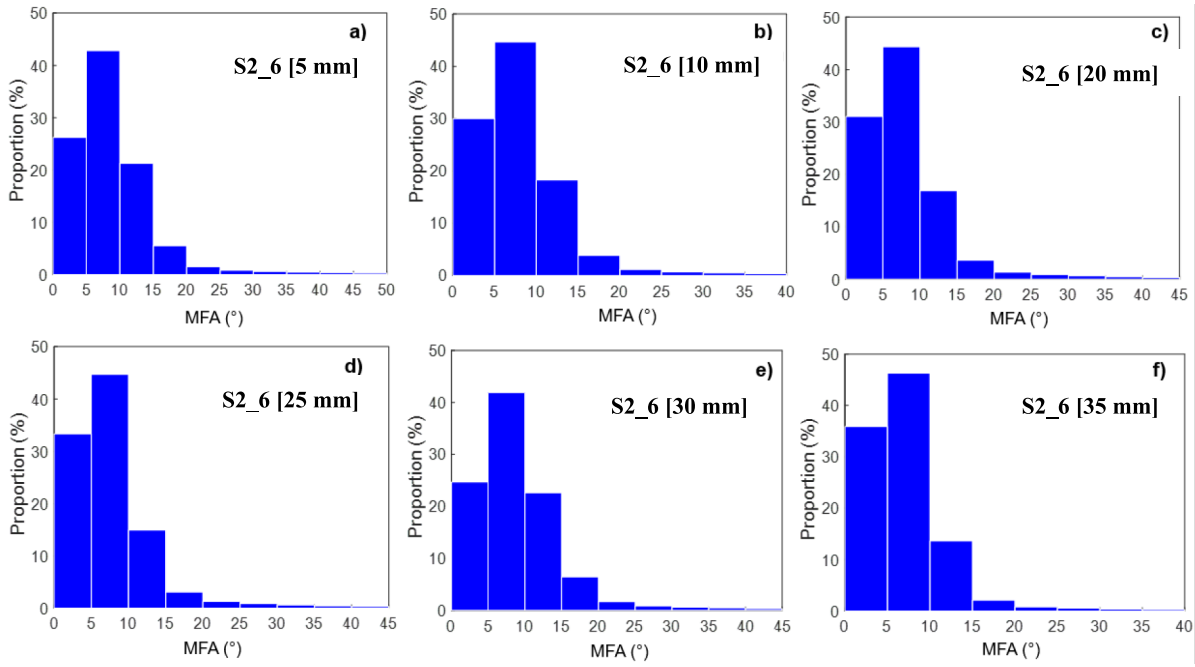

Fig. 14 Histograms of MFA distribution for six measurements carried out on sample S2_6 for various longitudinal positions

The longitudinal heterogeneity of the MFA volumetric fraction (Fig. 14) shows main differences in distributions observed for the [0°, 5°] and [10°, 15°] intervals while, similarly as in Fig. 13, it remains roughly constant in the [5°, 10°] range. This trend further confirms that the larger MFA decrease at the benefit of the smaller. As the most rigid element, and one whose microfibril orientation has a significant influence on the mechanical behaviour of plant fibre (Baley 2002; Placet et al. 2014a, b), this longitudinal variability of cellulose MFA could have a significant impact on the mechanical properties of fibre bundle samples. It is essential to emphasize that the sample used in this longitudinal study is a 50mm long fibre bundle. Over such a length, the fibre bundle may be made up of different fibres, resulting from the overlapping of several elementary fibres. One fibre bundle may include more than a dozen elementary fibres

(Charlet et al. 2007), it is then interesting to notice that the dispersion of MFA on a bundle is apparently not larger than the one in elementary fibers. A specific study on elementary fibres is in progress to test the variation at this scale.

MFA distribution evolution under tensile tests

The MFA distributions were also determined for each deformation level. The analysis of the corresponding histograms (Fig. 15) reveals that the majority of microfibril rearrangements occur in the MFA ranges 0–5° and 10–15°, while the fraction of microfibrils in the [5–10°] range is roughly constant or slightly increasing. During tensile loading, there is an increase of the volume fraction of microfibrils between [0°, 5°] and a decrease between [10°, 15°], indicating that overall, MFA decreases as the sample stretch along Z increases. The tensile application induces a reorientation of cellulose microfibrils along the sample axis with an increase in the volume fraction of microfibrils between 0 and 5° and to a lesser extent between 5 and 10°, while it decreases in the [10°, 15°] interval.

Samples S2_4 and S2_7 MFAs exhibit similar behaviours under tensile stress (Fig. 15a and b, with a slight and continuous increase of $T_{5\text{-}10}$, of the order of 1.9 and 3% from undeformed to 1.2% deformation respectively. However, the other MFA volume fractions behave

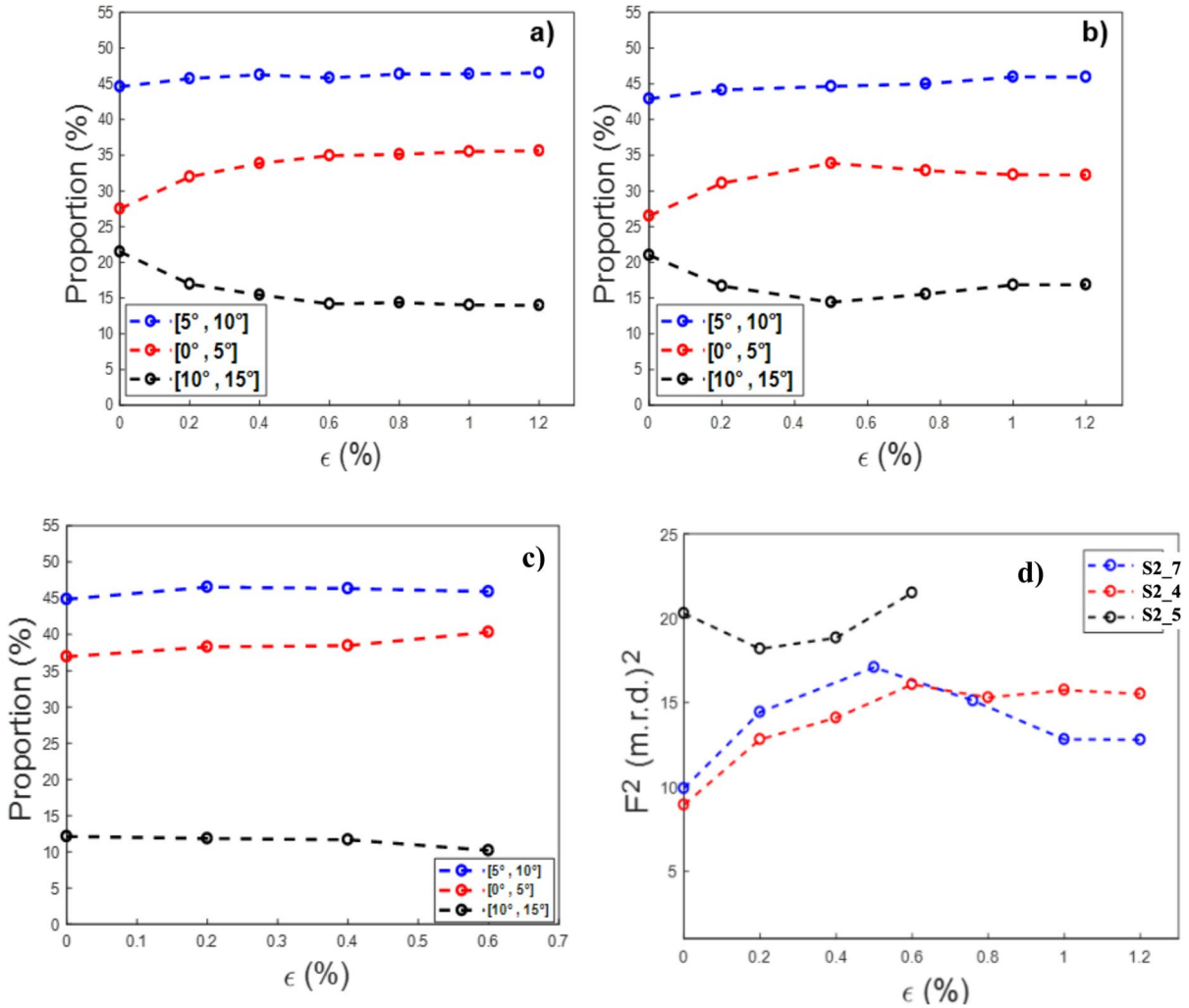

Fig. 15 For samples **a** S2_4, **b** S2_7 and **c** S2_5, evolution under tension (with a given ε applied strain) of microfibrils volumic fractions with orientations between [0°, 5°], [5°, 10°], and [10°, 15°] and **d** the corresponding texture strengths F^2

differently. A strong increase in $T_{0\text{-}5}$ is observed up to $\varepsilon = 0.3\%$, corresponding to 8.1 and 5.7% of the undeformed value respectively, and this increase is in phase with the decrease of $T_{10\text{-}15}$, by 7.5% and 4.13% respectively. It can be then concluded that the decrease in MFA during traction, and hence the reorientation of microfibrils, is non-linearly evolving with strain (Fig. 15a and b). First, an abrupt drop in MFA from undeformed to 0.2% strain happens, followed by a smaller drop, or even stabilization of MFAs beyond 0.6–0.8% strain. This increase, then stabilization, is also visible as a corresponding increase and stabilization of the overall texture strengths F^2 in S2_4 and S2_7 (Fig. 15d. Even if this 3-phase reorientation evolution seems to be coherent with the non-linear tensile behaviour of flax fibres, as the sample holder used does not measure the load, it is impossible to link this non-linear evolution of microfibril reorientation to the non-linearities of the tensile curve (stress–strain of flax). There is therefore a reorientation of the microfibrils along the Z axis of the sample, but it is preponderant during the first moments of the test before stabilizing as the strain increases. Although the 5° OD discretization step does not allow us to strictly determine the volume fraction of microfibrils whose MFA is very close to 0° at the end of tensile tests, the fraction of microfibrils for MFA larger than 5° is always more than 60%, whatever the deformation ratio and sample considered. In other words, there appears to be a limit value for reorientation, which according to the analysis (Fig. 15) would lie above 0.8% strain. This hypothesis can be compared with the findings of Kölln et al., (2005) and Riekel et al. (1999) who found a limiting value for the parameter describing preferred orientations for flax and Kevlar fibres respectively. This partial reduction in MFA during tensile stress has been shown for flax elementary fibres by Thuault (2011), or hemp fibre bundles by Placet et al. (2011a). Recent research involving in situ X-ray Diffraction under continuous tensile tests on flax elementary fibres reveals a variation in MFA during the test, with MFA decreases ranging from 3 to 24%, depending on the specific sample (Richely et al. 2022). However, these results were based on average MFA measurements. The approach presented here instead allows to quantify the variation in MFA distribution under tensile stress. The two-stage decrease observation in MFA of flax fibres under tension revealed by this distribution analysis is similar to the results of (Thuault 2011). Also, it should be emphasized that the strain rate can have an influence on microfibril rearrangement due to the viscoelastic nature of the polymeric components of the flax ultrastructure. However, because of the sample holder used in our tests, no strain rate was monitored at each deformed state. It would be then interesting in future studies to use experimental set-ups that would make it possible to associate the strain rate with each in situ tensile test.

For the third sample, S2_5, up to sample rupture for a maximum deformation of 0.6% (S2_5_0.6), Fig. 15c indicates that the MFA reorganizations in this sample are less significant than those in the samples S2_4 and S2_7 within the same deformation range. Compared to samples S2_4 and S2_7, the evolution of volume fractions for all three MFA intervals is weak, with 3.4% and 1% increases between [0°,5°] and [5°,10°], respectively, and only 1% decrease for the interval [10°,15°]. These modest reorientations are likely due to the relatively high fraction of initially oriented microfibrils between [0°,5°] in the undeformed state, compared to S2_4 and S2_7 (37% for sample S2_5, and around 27% for S2_4 and S2_7). The initial $T_{0\text{-}5}$ of S2_5 (37%) is larger than the largest $T_{0\text{-}5}$ values of S2_4 and S2_7. This is coherent with a limit value of reorientation of microfibrils during tensile tests, and with the impossibility to reorient microfibrils already aligned close to Z. (Richely et al. 2022) have also shown that under tensile loading, flax elementary fibres with initially large MFAs tend to exhibit larger reorientation of the microfibrils along the tensile axis. This variation in MFA distribution behaviour during tensile test may also arise from poor alignment of the sample along the tensile axis, as noted by (Richely et al. 2022). Improper alignment of a sample can induce additional shear, which could impact the ability of microfibrils to realign within the surrounding polymeric matrix, thereby contributing to the observed disparities between the samples. Similarly, the ability of the matrix to facilitate microfibril reorientation can vary from sample to sample, and even along the same sample.

Conclusively, we observe on one hand that it exists a limit reorientation of microfibrils upon deformation, after which no significant further reorientation occurs, and on the other hand, that this reorientation favours $T_{0\text{-}5}$ at the expense of $T_{10\text{-}15}$. These two observations seem to imply that there exists some equilibrium and/or pinning force imposing on microfibrils adopting a MFA in the 5–10° range.

Characterization of the so-called paracrystalline cellulose

Facing the difficulty in modelling the paracrystalline structure, even using a March Dollase texture correction model (generally not suitable to represent the ODF), Duchemin 2017 proposed the use of another allomorph of cellulose, cellulose IV_I, to describe this paracrystalline phase. However, after several refinement attempts, we could not find any experimental data attesting for the presence of this allomorph in our plant fibres, and in flax, no data exist that have revealed its existence to our knowledge. We have then chosen in this work to retain cellulose Iβ to model the paracrystalline structure, using isotropic crystallite sizes and a fibre texture described with the standard function model. The obtained refined cell parameter values are clearly larger than to the ones refined for the crystalline phase (Table 8), and the angle γ is systematically lower than 96.5°. Such a difference from the $I\beta$ crystal structure suggests that we might be dealing with a slightly different type of cellulose. However, since the exact ultrastructure of the paracrystalline regions is still poorly defined, we cannot opt for another choice, and the actual model satisfies good refinements. It is rather reassuring that the paracrystalline structure does not depart too much from that of cellulose Iβ and provides with satisfactory XRD fits, as asserted by the obtained R_{wp} values (Table 8).

The refined spherical crystallite shapes of the paracrystalline phase are found in the 0.65 to 2.13nm range. For sample S1_4 (Series 1) the refined shape of 0.65nm, value smaller than the cellulose Iβ lattice parameters, shows that the corresponding phase can be considered as fully amorphous. Comparing these values with literature data, Duchemin et al. (2017) found similar values (between 1.4 and 2.1nm) using Rietveld analysis using the cellulose IV_I allomorph.

Concerning preferred orientations, the paracrystalline phase exhibits a marked 90% Lorentzian character, whereas the crystalline Iβ texture has a marked Gaussian character. Moreover, the texture strength of the paracrystalline phase is smaller, with orientation distribution maxima between 9 and 42 m.r.d, corresponding to a larger angular dispersion of the c-axes with respect to Z (Fig. 16), up to 45°.

This quantitative texture analysis seems to confirm the existence in our samples of an intermediate paracrystalline phase in flax cellulose (Bourmaud et al. 2019; Duchemin et al. 2012), neither fully amorphous nor perfectly crystalline. Speaking about crystallographic texture of a fully amorphous phase would have no meaning, but the "paracrystalline cellulose" still exhibits cell parameters with

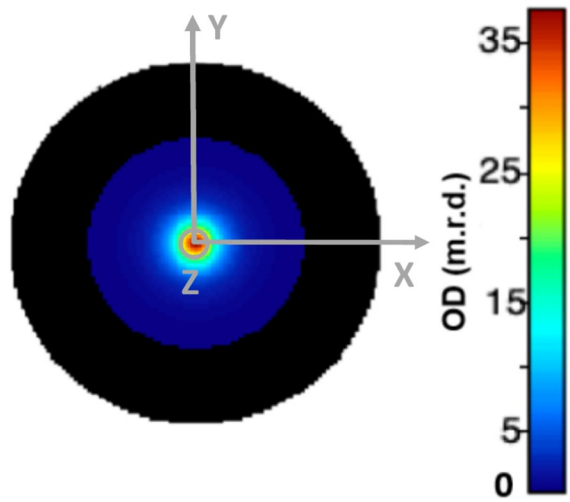

Fig. 16 Typical paracrystalline cellulose {001} pole figure

Table 8 Lattice parameters, isotropic crystallite sizes D_{iso} and factors R_{wp} of Series 2 samples corresponding to the refinement of 65 diffraction spectra. Values in brackets are standard deviations on the last digit as 1σ given by MAUD

Paracrystalline phase, Series 2						
Samples	a(Å)	b(Å)	c(Å)	γ(°)	D_{iso} (nm)	R_{wp}(%)
S2_1	9.1 (4)	12.4 (1)	10.84 (9)	93 (2)	2.02 (4)	26.13
S2_2	9.11 (4)	12.30 (1)	10.8 (1)	92 (2)	2.03 (6)	31.26
S2_3	9.28 (5)	11.8 (1)	10.9 (2)	94 (2)	2.13 (7)	29.46
S2_4	8.66 (4)	9.23 (8)	10.56 (9)	96 (1)	1.94 (3)	23.00
S2_5	8.93 (8)	10.7 (2)	10.5 (2)	86 (3)	1.98 (8)	26.37
S2_6	8.90 (5)	8.6 (1)	10.5 (1)	79.8 (1)	2.04 (4)	21.75
S2_7	8.95 (6)	8.8 (1)	10.4 (1)	81 (1)	2.0 (5)	24.55

crystallites composed of few unit-cells, as usually met in nanocrystals. As such, this phase could also be called nanocrystalline Iβ, as far as XRD is of concerns. Our results suggest that the paracrystalline cellulose chains are initially oriented, which would explain the absence of sharp diffraction peaks in the patterns (Fig. 8), but a rather high orientation value. This pre-orientation of flax paracrystalline cellulose chains was suggested by (Astley and Donald 2003). Also, the work of (Duchemin et al. 2012) revealed that paracrystalline cellulose chains are located at the interface where the non-cellulosic components of flax fibres adhere to the surfaces of cellulose crystallites, contributing to the strong adhesion observed between cellulose crystallites, hemicelluloses and pectins in flax. The presence of the paracrystalline phase would then explain why the non-crystalline contribution to the diffractogram has a more complex shape (Fig. 8) than the simple Gaussian orientation distribution.

Our study suggests that the paracrystalline phase is probably a gradual transition phase between the disorder of the "classic amorphous phase" and the order of the crystalline phase. Even in artificial polymers such as PET (polyethylene terephthalate), the existence of a third phase continuum between perfectly crystalline and more or less oriented amorphous zones has been demonstrated by several authors (Fischer & Fakirov 1976; Rastogi et al. 2004). This identification of a possible paracrystalline phase in flax by Combined Analysis is important because, unlike crystalline cellulose for which direct evidence (transmission electron microscopy, atomic force microscopy) can be gathered, the exact ultrastructure of paracrystalline regions is still poorly documented. Nevertheless, refined lattice parameters for this paracrystalline structure strongly differ from those of (Nishiyama et al. 2002), resulting in quite different peak positions (Fig. 8). Further analysis is required to validate the assigned crystallographic structure.

Conclusion

In this work, the characterization of flax ultrastructure using X-ray diffraction Combined Analysis, provided initial information to deepen the understanding of the structure, microstructure and texture of flax fibres. The biphasic model initially used to describe the well-known semi-crystallinity of flax has revealed the possible existence of a paracrystalline phase, which serves as a transitional phase between an amorphous phase and a crystalline phase. The quantitative texture analysis shows that flax fibres exhibit a $<001>$ fibre texture with microfibrils of the crystalline Iβ phase having a tilt angle distribution with respect to the fibre axis in the 0 and 20° range and exhibiting a maximum of the distribution (MFA values) in the 5° to 10° interval range. Moreover, the longitudinal evolution of the MFA shows that it is difficult to assign a unique MFA for a fibre bundle and as shown by Melelli et al. (2020a) for elementary fibres.

The microstructure analysis revealed that Iβ cellulose microfibrils have an elongated ellipsoidal shape along the c-axis of the crystal lattice, aligned with the direction of fibre texture.

Under tensile loading for two samples (up to 1.2% strain corresponding to fibre rupture), a significant decrease in MFA with increasing strain is observed, confirming the reorientation of cellulose microfibrils along the strained fibre axis and reinforcing the preferential orientations of the crystallites. However, this texture evolution appears to be more pronounced for strains below 0.6% and is relatively weak or attenuated for strains above this. In contrast to these two samples, the third sample observed up to 0.6% strain is characterized by a rather weak MFA evolution. As no clear evolution of crystallite dimensions and crystallinity is evidenced under tensile loading, this seems to exclude the hypothesis of stress recrystallization of paracrystalline cellulose in our studied samples, but more associated to texture strengthening. Moreover, further works related to an optimisation of our microtraction holder are underway in order to be able to correlate the strain rate with each in situ-tensile test. Complementary works on elementary fibers and using this X-ray combined analysis approach are in progress and will be also supplemented by polarised second harmonic generation microscopy characterizations.

Acknowledgments We sincerely want to thank Pr Jean-Christophe Baloche (IUT Caen) for sample holders 3D printings. The Chevreul Institute is thanked for its help in the development of this work through the ARCHI-CM project supported by the "Ministère de l'Enseignement Supérieur de la Recherche et de l'Innovation", the region "Hauts-de-France", the ERDF program of the European Union and the "Métropole Européenne de Lille".

Author contributions M.M. supervised this research, exploited the measurements and wrote the manuscript. K.G. conducted this research, exploited the measurements and wrote

the manuscript. C.P. and F.G. co-supervised this research. O.P. and G. S. performed XRD measurements. DC implemented the QTA discussion and analysis. L.L. helped through the use of his MAUD program to the refinements. All authors read and approved the manuscript.

Funding The authors declare that no funds, grants, or other support were received during the preparation of this manuscript.

Data availability Data sets generated during the current study are available from the corresponding author on reasonable request.

Declarations

Conflict of interest The authors declare no competing interests.

Ethical approval This work was carried out in compliance with ethical standards.

References

Agarwal UP (2009) Raman spectroscopic characterization of wood and pulp fibers. Charact Lignocellulosic Mater. https://doi.org/10.1002/9781444305425.ch2

Andersson S, Serimaa R, Paakkari T, Saranpää P, Pesonen E (2003) Crystallinity of wood and the size of cellulose crystallites in Norway spruce (*Picea abies*). J Wood Sci 49(6):531–537. https://doi.org/10.1007/s10086-003-0518-x

Aslan M, Chinga-Carrasco G, Sørensen BF, Madsen B (2011) Strength variability of single flax fibres. J Mater Sci 46(19):6344–6354. https://doi.org/10.1007/s10853-011-5581-x

Astley OM, Donald AM (2001) A small-angle X-ray scattering study of the effect of hydration on the microstructure of flax fibers. Biomacromol 2(3):672–680. https://doi.org/10.1021/bm005643l

Astley OM, Donald AM (2003) The tensile deformation of flax fibres as studied by X-ray scattering. J Mater Sci 38(1):165–171. https://doi.org/10.1023/A:1021186421194

Atalla RH, VanderHart DL (1999) The role of solid state ^{13}C NMR spectroscopy in studies of the nature of native celluloses. Solid State Nucl Mag 15(1):1–19. https://doi.org/10.1016/S0926-2040(99)00042-9

Baley C (2002) Analysis of the flax fibres tensile behaviour and analysis of the tensile stiffness increase. Compos Part A Appl Sci Manuf 33:939–948. https://doi.org/10.1016/S1359-835X(02)00040-4

Baley C, Bourmaud A (2014) Average tensile properties of French elementary flax fibers. Mater Lett 122:159–161. https://doi.org/10.1016/j.matlet.2014.02.030

Baley C, Morvan C, Grohens Y (2005) Influence of the absorbed water on the tensile strength of flax fibers. Macromol Symp 222:195–202. https://doi.org/10.1002/masy.200550425

Balzar D, Audebrand N, Daymond MR, Fitch A, Hewat A, Langford JI, Le Bail A, Loue D, Masson O, McCowan CN, Popa NC, Stephens PW, Toby BH (2004) Size–strain line-broadening analysis of the ceria round-robin sample. Appl Crystallogr 37:911–924. https://doi.org/10.1107/S0021889804022551

Bayer EA, Chanzy H, Lamed R, Shoham Y (1998) Cellulose, cellulases and cellulosomes. Curr Opin Struct Biol 8(5):548–557. https://doi.org/10.1016/S0959-440X(98)80143-7

Bourmaud A, Morvan C, Bouali A, Placet V, Perré P, Baley C (2013) Relationships between micro-fibrillar angle, mechanical properties and biochemical composition of flax fibers. Ind Crops Prod 44:343–351. https://doi.org/10.1016/j.indcrop.2012.11.031

Bourmaud A, Siniscalco D, Foucat L, Goudenhooft C, Falourd X, Pontoire B, Arnould O, Beaugrand J, Baley C (2019) Evolution of flax cell wall ultrastructure and mechanical properties during the retting step. Carbohydr Polym 206:48–56. https://doi.org/10.1016/j.carbpol.2018.10.065

Bu L, Himmel ME, Crowley MF (2015) The molecular origins of twist in cellulose I-beta. Carbohydr Polym 125:146–152. https://doi.org/10.1016/j.carbpol.2015.02.023

Cave ID (1997a) Theory of X-ray measurement of microfibril angle in wood Part 1. The condition for reflection X-ray diffraction by materials with fibre type symmetry. Wood Sci Technol 31(3):143–152. https://doi.org/10.1007/BF00705881

Cave ID (1997b) Theory of X-ray measurement of microfibril angle in wood: Part 2 The diffraction diagram X-ray diffraction by materials with fibre type symmetry. Wood Sci Technol 31(4):225–234. https://doi.org/10.1007/BF00702610

Charlet K, Baley C, Morvan C, Jernot J-P, Gomina M, Bréard J (2007) Characteristics of Hermès flax fibres as a function of their location in the stem and properties of the derived unidirectional composites. Compos Part A Appl Sci Manuf 38:1912–1921. https://doi.org/10.1016/j.compositesa.2007.03.006

Charlet K, Jernot J-P, Bréard J, Gomina M (2010a) Scattering of morphological and mechanical properties of flax fibres. Ind Crop Prod 32:220–224. https://doi.org/10.1016/j.indcrop.2010.04.015

Charlet K, Jernot J-P, Eve S, Gomina M, Bréard J (2010b) Multi-scale morphological characterisation of flax: from the stem to the fibrils. Carbohydr Polym 82(1):54–61. https://doi.org/10.1016/j.carbpol.2010.04.022

Chateigner D (2005) Reliability criteria in quantitative texture analysis with experimental and simulated orientation distributions. J Appl Crystallogr. https://doi.org/10.1107/S0021889805013695

Chateigner D, Lutterotti L & Morales M (2019) Quantitative texture analysis and combined analysis. In C J Gilmore, J A Kaduk & H Schenk (Éds.), *Powder diffr: Vol. H* pp. 555-580.

Clair B, Déjardin A, Pilate G, Alméras T (2018) Is the G-layer a tertiary cell wall? Front Plant Sci 9:8–11. https://doi.org/10.3389/fpls.2018.00623

De Souza Lima MM, Borsali R (2004) Rodlike cellulose microcrystals: structure, properties, and applications.

Macromol Rapid Commun 25(7):771–787. https://doi.org/10.1002/marc.200300268
Ding SY, Himmel ME (2006) The maize primary cell wall microfibril: a new model derived from direct visualization. J Agric Food Chem 54(3):597–606. https://doi.org/10.1021/jf051851z
Ding SY, Zhao S, Zeng Y (2014) Size, shape, and arrangement of native cellulose fibrils in maize cell walls. Cellulose 21(2):863–871. https://doi.org/10.1007/s10570-013-0147-5
Donaldson L, Xu P (2005) Microfibril orientation across the secondary cell wall of Radiata pine tracheids. Trees Struct Funct 19(6):644–653. https://doi.org/10.1007/s00468-005-0428-1
Driemeier C (2014) Two-dimensional Rietveld analysis of celluloses from higher plants. Cellulose 21(2):1065–1073. https://doi.org/10.1007/s10570-013-9995-2
Driemeier C, Calligaris GA (2011) Theoretical and experimental developments for accurate determination of crystallinity of cellulose i materials. J Appl Crystallogr 44(1):184–192. https://doi.org/10.1107/S0021889810043955
Duchemin B (2017) Size, shape, orientation and crystallinity of cellulose Iβ by X-ray powder diffraction using a free spreadsheet program. Cellulose 24(7):2727–2741. https://doi.org/10.1007/s10570-017-1318-6
Duchemin B, Thuault A, Vicente A, Rigaud B, Fernandez C, Eve S (2012) Ultrastructure of cellulose crystallites in flax textile fibres. Cellulose 19(6):1837–1854. https://doi.org/10.1007/s10570-012-9786-1
Fink HP, Walenta E, Kunze J (1999) Structure of natural cellulosic fibres. Part 2. The supermolecular structure of bast fibres and their changes by mercerization as revealed by X-ray diffraction and 13C-NMR-spectroscopy. Paper 53(9):534–542
Fischer EW, Fakirov S (1976) Structure and properties of polyethyleneterephthalate crystallized by annealing in the highly oriented state: Part 1 Morphological structure as revealed by small-angle X-ray scattering. J Mat Sci 11(6):1041–1065. https://doi.org/10.1007/BF02396639
Garat W, Corn S, Le Moigne N, Beaugrand J, Bergeret A (2018) Analysis of the morphometric variations in natural fibres by automated laser scanning: towards an efficient and reliable assessment of the cross-sectional area. Compos A Appl Sci Manuf 108:114–123. https://doi.org/10.1016/j.compositesa.2018.02.018
Gierlinger N, Luss S, König C, Konnerth J, Eder M, Fratzl P (2010) Cellulose microfibril orientation of *Picea abies* and its variability at the micron-level determined by Raman imaging. J Exp Bot 61(2):587–595. https://doi.org/10.1093/jxb/erp325
Gogoli K, Gehring F, Poilâne C, Morales M (2021) Analysis of morphological variations of flax fibre bundles by Fraunhofer diffraction. Ind Crop Prod 171:113856. https://doi.org/10.1016/j.indcrop.2021.113856
Gogoli K (2022) Contribution à l'étude des faisceaux de fibres de lin : Analyse des relations morphologie-comportement mécanique-ultrastructure. Dissertation, Université de Caen -Normandie, France
Gomez-Campos A, Vialle C, Rouilly A, Sablayrolles C, Hamelin L (2021) Flax fiber for technical textile: a life cycle inventory. J Clean Prod 281:12517. https://doi.org/10.1016/j.jclepro.2020.125177
Gorshkova T, Morvan C (2006) Secondary cell-wall assembly in flax phloem fibres: role of galactans. Planta 223(2):149–158
Gorshkova T, Chernova T, Mokshina N, Ageeva M, Mikshina P (2018) Plant 'muscles' : Fibers with a tertiary cell wall. New Phytol 218(1):66–72. https://doi.org/10.1111/nph.14997
Gražulis S, Chateigner D, Downs RT, Yokochi AT, Quiros M, Lutterotti L, Manakova E, Butkus J, Moeck P, Le Bail A (2009) Crystallography open database – an open-access collection of crystal structures. J Appl Crystallogr 42:726–729. https://doi.org/10.1107/S0021889809016690
Haag K, Müssig J (2016) Scatter in tensile properties of flax fibre bundles: influence of determination and calculation of the cross-sectional area. J Mater Sci 51(17):7907–7917. https://doi.org/10.1007/s10853-016-0052-z
Hamad WY, Hu TQ (2010) Structure-process-yield interrelations in nanocrystalline cellulose extraction. Can J Chem Eng 88(3):392–402. https://doi.org/10.1002/cjce.20298
Hill RJ, Flack HD (1987) The use of the Durbin-Watson d statistic in Rietveld analysis. J Appl Crystallogr 20(5):356–361. https://doi.org/10.1107/S0021889887086485
Hosemann R, Hindeleh AM (1995) Structure of crystalline and paracrystalline condensed matter. J Macromol Sci B 34(4):327–356. https://doi.org/10.1080/00222349508219497
Jarvis M (2003) Cellulose stacks up. Nature 426(6967):611–612. https://doi.org/10.1038/426611a
John M, Thomas S (2008) Biofibres and biocomposites. Carbohydr Polym 71(3):343–364. https://doi.org/10.1016/j.carbpol.2007.05.040
Kölln K, Grotkopp I, Burghammer M, Roth SV, Funari SS, Dommach M, Müller M (2005) Mechanical properties of cellulose fibres and wood. Orientational aspects in situ investigated with synchrotron radiation. J Synchrotron Radiat 12:239–244
Kulshreshtha AK, Patil NB, Dweltz NE, Radhakrishnan T (1969) Axial order in ramie. Text Res J 39(12):1158–1161. https://doi.org/10.1177/004051756903901211
Le Bail A (1995) Modelling the silica glass structure by the Rietveld method. J Non-Cryst Solids 183(1-2):39–42. https://doi.org/10.1016/0022-3093(94)00664-4
Le Bail A (2005) Whole powder pattern decomposition methods and applications: a retrospection. Powder Diffr 20(4):316–326. https://doi.org/10.1154/1.2135315
Lehtiö J, Sugiyama J, Gustavsson M, Fransson L, Linder M, Teeri TT (2003) The binding specificity and affinity determinants of family 1 and family 3 cellulose binding modules. Proc Natl Acad Sci USA 100(2):484–489. https://doi.org/10.1073/pnas.212651999
Lennholm H, Larsson T, Iversen T (1994) Determination of cellulose Iα and Iβ in lignocellulosic materials. Carbohyd Res 261(1):119–131. https://doi.org/10.1016/0008-6215(94)80011-1
Leppänen K, Andersson S, Torkkeli M, Knaapila M, Kotelnikova N, Serimaa R (2009) Structure of cellulose and microcrystalline cellulose from various wood species, cotton and flax

studied by X-ray scattering. Cellulose 16(6):999–1015. https://doi.org/10.1007/s10570-009-9298-9

Ling Z, Wang T, Makarem M, Santiago Cintrón M, Cheng HN, Kang X, Bacher M, Potthast A, Rosenau T, King H, Delhom CD, Nam S, Vincent Edwards J, Kim SH, Xu F, French AD (2019) Effects of ball milling on the structure of cotton cellulose. Cellulose 26(1):305–328. https://doi.org/10.1007/s10570-018-02230-x

Long JM, Conn AB, Batchelor AWJ, Evans R (1998) Comparison of methods to measure fibril angle in wood fibres. APPITA Annual General Conference 1:23–26

Lutterotti L (2012) Quantitative phase analysis: method developments. Nato Sci Peace Sec B. https://doi.org/10.1007/978-94-007-5580-2_21

Lutterotti L, Matthies S, Wenk HR, Schultz AS, Richardson JW (1997) Combined texture and structure analysis of deformed limestone from time-of-flight neutron diffraction spectra. J Appl Phys 81(2):594–600. https://doi.org/10.1063/1.364220

Lutterotti L, Bortolotti M, Ischia G, Lonardelli I, Wenk HR (2007) Rietveld texture analysis from diffraction images. Z Kristallogr, Supplement 1(26):125–130. https://doi.org/10.1524/zksu.2007.2007.suppl_26.125

Lutterotti L, Vasin R, Wenk HR (2014) Rietveld texture analysis from synchrotron diffraction images. I. Calibration and basic analysis. Powder Diffr 29(1):76–84. https://doi.org/10.1017/S0885715613001346

Marts RO (1955) Fluorescence microscopy for measuring fibril angles in pine tracheids. Biotech Histochem 30(5):243–248. https://doi.org/10.3109/10520295509114473

Matthies S, Helming K, Steinkopff T, Kunze K (1988) Standard distributions for the case of fibre textures. Phys Status Solidi B 150(1):K1–K5. https://doi.org/10.1002/pssb.2221500137

Melelli A, Arnould O, Beaugrand J, Bourmaud A (2020a) The middle lamella of plant fibers used as composite reinforcement : investigation by atomic force microscopy. Molecules. https://doi.org/10.3390/molecules25030632

Melelli A, Jamme F, Legland D, Beaugrand J, Bourmaud A (2020b) Microfibril angle of elementary flax fibres investigated with polarised second harmonic generation microscopy. Ind Crops Prod 156:112847. https://doi.org/10.1016/j.indcrop.2020.112847

Melelli A, Durand S, Arnould O, Richely E, Guessasma S, Jamme F, Beaugrand J, Bourmaud A (2021) Extensive investigation of the ultrastructure of kink-bands in flax fibres. Ind Crop Prod. https://doi.org/10.1016/j.indcrop.2021.113368

Morgillo L, Goudenhooft C, Melelli A, Durand S, Abida M, Beauregrang J, Bourmaud A (2025) Impact of flax fibre kink-bands on local longitudinal mechanical properties and cell wall ultrastructure. Compos Part A 196:108990. https://doi.org/10.1016/j.compositesa.2025.108754

Morvan C, Andème-Onzighi C, Girault R, Himmelsbach DS, Driouich A, Akin DA (2003) Building flax fibres: more than one brick in the walls. Plant Physiol Biochem 41:935–944. https://doi.org/10.1016/j.plaphy.2003.07.001

Muller M, Czihak C, Vogl G, Fratzl P, Schober H, Riekel C (1998) Direct observation of microfibril arrangement in a single native cellulose fiber by microbeam small-angle X-ray scattering. Macromolecules 31:3953–3957

Müller M, Czihak C, Burghammer M, Riekel C (2000) Combined X-ray microbeam small-angle scattering and fibre diffraction experiments on single native cellulose fibres. J Appl Crystallogr 33(3 I):817–819. https://doi.org/10.1107/S0021889800099751

Müller M, Murphy B, Burghammer M, Riekel C, Roberts M, Papiz M, Clarke D, Gunneweg J, Pantos E (2004) Identification of ancient textile fibres from Khirbet Qumran caves using synchrotron radiation microbeam diffraction. Spectrochim Acta B 59(10–11):1669–1674. https://doi.org/10.1016/j.sab.2004.07.018

Newman RH, Hill SJ, Harris PJ (2013) Wide-angle X-ray scattering and solid-state nuclear magnetic resonance data combined to test models for cellulose microfibrils in mung bean cell walls. Plant Physiol 163(4):1558–1567. https://doi.org/10.1104/pp.113.228262

Nishiyama Y, Langan P, Chanzy H (2002) Crystal structure and hydrogen-bonding system in cellulose 1 beta from synchrotron X-ray and neutron fiber diffraction. J Am Chem Soc 124(31):9074–9082

Nishiyama Y, Sugiyama J, Chanzy H, Langan P (2003) Crystal structure and hydrogen bonding system in cellulose Iα from synchrotron X-ray and neutron fiber diffraction. J Am Chem Soc 125(47):14300–14306. https://doi.org/10.1021/ja037055w

Oehme DP, Doblin MS, Wagner J, Bacic A, Downton MT, Gidley MJ (2015) Gaining insight into cell wall cellulose macrofibril organisation by simulating microfibril adsorption. Cellulose 22(6):3501–3520. https://doi.org/10.1007/s10570-015-0778-9

Oliveira RP, Driemeier C (2013) CRAFS: a model to analyze two-dimensional X-ray diffraction patterns of plant cellulose. J Appl Crystallogr 46(4):1196–1210. https://doi.org/10.1107/S0021889813014805

Placet V, Bouali A, Perré P (2011b) The possible role of microfibril angle of Hemp fibre during fatigue tests and its determination using wide-angle X-ray diffraction. Materiaux Tech 99(6):683–689. https://doi.org/10.1051/mattech/2011120

Placet V, Cissé O, Boubakar L (2014a) Nonlinear tensile behaviour of elementary hemp fibres. Part I: investigation of the possible origins using repeated progressive loading with in situ microscopic observations. Compos Part A-Appl S 56:319–327. https://doi.org/10.1016/j.compositesa.2012.11.019

Placet V, Bouali A, Garcin C, Cote J M & Perré P (2011) Suivi par DRX des réarrangements microstructuraux induits par sollicitations mécaniques dans les fibres végétales tirées du chanvre. *CFM 2011 - 20ème Congrès Français de Mécanique*: 1-8.

Placet V, Trivaudey F, Cisse O & Boubakar M L (2013) What are the possible origins of the nonlinear tensile behaviour of hemp fibres? *ICCM International Conferences on Composite Materials*, *2013-July*: 5981-5988. https://www.scopus.com/inward/record.uri?eid=2-s2.0-84958865000&partnerID=40&md5=1ea50accc3360411c07e97fb68470340

Placet V, Trivaudey F & Boubakar M L (2014) *Fibre végétale isolée, microstructure, caractérisation experimentale, et modélisation*: 1-10

Popa NC (1992) Texture in rietveld refinement. J Appl Crystallogr 25(5):611–616. https://doi.org/10.1107/S0021889892004795

Popa NC (1998) The (hkl) dependence of diffraction-line broadening caused by strain and size for all Laue groups in rietveld refinement. J Appl Crystallogr 31(2):176–180. https://doi.org/10.1107/S0021889897009795

Raj G, Balnois E, Baley C, Grohens Y (2011) Role of polysaccharides on mechanical and adhesion properties of flax fibres in Flax/PLA biocomposite. Int J Polym Sci 2011:1–11. https://doi.org/10.1155/2011/503940

Rastogi R, Vellinca WP, Rastogi S, Schick C, Meijer HEH (2004) The three-phase structure and mechanical properties of poly(ethylene terephthalate). J Polym Sci Pol Phys 42(11):2092–2106. https://doi.org/10.1002/polb.20096

Richely E, Bourmaud A, Placet V, Guessasma S, Beaugrand J (2021a) A critical review of the ultrastructure, mechanics and modelling of flax fibres and their defects. Prog Mater Sci. https://doi.org/10.1016/j.pmatsci.2021.100851

Richely E, Durand S, Melelli A, Kao A, Magueresse A, Dhakal H, Gorshkova T, Callebert F, Bourmaud A, Beaugrand J, Guessasma S (2021b) Novel insight into the intricate shape of flax fibre lumen. Fibers 9(4):1–17. https://doi.org/10.3390/fib9040024

Richely E, Nuez L, Pérez J, Rivard C, Baley C, Bourmaud A, Guessasma S, Beaugrand J (2022) Influence of defects on the tensile behaviour of flax fibres: cellulose microfibrils evolution by synchrotron X-ray diffraction and finite element modelling. Compos Part c: Open Access 9:100300. https://doi.org/10.1016/j.jcomc.2022.100300

Riekel C, Dieing T, Engström P, Vincze L, Martin C, Mahendrasingam A (1999) X-ray microdiffraction study of chain orientation in poly(p-phenylene terephthalamide). Macromolecules 32(23):7859–7865. https://doi.org/10.1021/ma990267m

Rietveld HM (1969) A profile refinement method for nuclear and magnetic structures. J Appl Crystallogr 2:65–71. https://doi.org/10.1107/S0021889892004795

Rihouey C, Paynel F, Gorshkova T, Morvan C (2017) Flax fibers : assessing the non-cellulosic polysaccharides and an approach to supramolecular design of the cell wall. Cellulose 24(5):1985–2001. https://doi.org/10.1007/s10570-017-1246-5

Roig F (2011) *Transitions et dynamique relaxationnelle de polymères issus de la paroi végétale* Dissertation. Université Toulouse III - Paul Sabatier, France

Roland JC, Mosiniak M, Roland D (1995) Dynamique du positionnement de la cellulose dans les parois des fibres textiles du lin (Linum usitatissimum). Acta Bot Gallica 142(5):463–484. https://doi.org/10.1080/12538078.1995.10515271

Saxe F, Eder M, Benecke G, Aichmayer B, Fratzl P, Burgert I, Rüggeberg M (2014) Measuring the distribution of cellulose microfibril angles in primary cell walls by small angle X-ray scattering. Plant Method 10:25. https://doi.org/10.1186/1746-4811-10-25

Saxena I, Brown RMJ (2005) Cellulose biosynthesis: current views and evolving concepts. Ann Bot-London 96(1):9–21

Thomas LH, Trevor Forsyth V, Šturcová A, Kennedy CJ, May RP, Altaner CM, Apperley DC, Wess TJ, Jarvis MC (2013) Structure of cellulose microfibrils in primary cell walls from collenchyma. Plant Physiol 161(1):465–476. https://doi.org/10.1104/pp.112.206359

Thuault A (2011) *Approche multi-échelle de la structure et du comportement mécanique de la fibre de lin*. Dissertation, Université de Caen Basse-Normandie - France

Thygesen A, Oddershede J, Lilholt H, Thomsen AB, Ståhl K (2005) On the determination of crystallinity and cellulose content in plant fibres. Cellulose 12(6):563–576. https://doi.org/10.1007/s10570-005-9001-8

Thygesen LG, Eder M, Burgert I (2007) Dislocations in single hemp fibres-investigations into the relationship of structural distortions and tensile properties at the cell wall level. J Mater Sci 42(2):558–564. https://doi.org/10.1007/s10853-006-1113-5

Toby BH (2006) R factors in Rietveld analysis: how good is good enough? Powder Diffr 21:67–70. https://doi.org/10.1154/1.2179804

Viljanen M, Suomela JA, Svedström K (2022) Wide-angle X-ray scattering studies on contemporary and ancient bast fibres used in textiles – ultrastructural studies on stinging nettle. Cellulose 29(4):2645–266. https://doi.org/10.1007/s10570-021-04400-w

Wang C, Wang N, Liu S, Choo-Simth LP, Zhang H, Zhi Z (2020) Investigation of microfibril angle of flax fibers using X-ray diffraction and scanning electron microscopy. J Nat Fibers 17(7):1001–1010. https://doi.org/10.1080/15440478.2018.1546639

Wardrop AB, Preston RD (1947) Organisation of the cell walls of tracheids and wood fibres. Nature 160(4078):911–913. https://doi.org/10.1038/160911a0

Zuckerstätter G, Schild G, Wollboldt P, Röder T, Weber HK, Sixta H (2009) The elucidation of cellulose supramolecular structure by 13C CP-MAS NMR. Lenzinger Ber 87:38–46